Structural evolution during cyclic glacier surges 2

Clarke, Garry K. C.; Hambrey, Michael

Published in:
Journal of Geophysical Research: Earth Surface

DOI:
10.1029/2018JF004870

Publication date:
2019

Citation for published version (APA):
Clarke, G. K. C., & Hambrey, M. (2019). Structural evolution during cyclic glacier surges 2: Numerical Modeling. *Journal of Geophysical Research: Earth Surface*, *124*(2), 495-525. https://doi.org/10.1029/2018JF004870

Structural evolution during cyclic glacier surges: 2. Numerical modeling

Garry K. C. Clarke[1] and Michael J. Hambrey[2]

Garry Clarke, clarke@eoas.ubc.ca

[1]Department of Earth, Ocean and Atmospheric Sciences, University of British Columbia, Vancouver, British Columbia, Canada.

[2]Centre for Glaciology, Department of Geography and Earth Sciences, Aberystwyth University, Aberystwyth, Ceredigion, United Kingdom.

This article has been accepted for publication and undergone full peer review but has not been through the copyediting, typesetting, pagination and proofreading process, which may lead to differences between this version and the Version of Record. Please cite this article as doi: 10.1029/2018JF004870

Abstract. The mesoscale structures of a glacier express the history of flow, temperature, and stress. Thus, in principle, numerical ice dynamics models have sufficient physics to examine the formation and transport of these structures. In this study we use a vertically integrated thermomechanical ice dynamics model to simulate the temporally evolving patterns of surficial moraine, stratification, foliation, and folding of glacier ice, and the density and orientation of traces of former crevasses. The modeled glaciers are simplified versions of Trapridge Glacier in northwest Canada that allow diagnostic modeling of influences on glacier structure and help to clarify the physics and numerics. In the model, surges occur every 50 years in response to a prescribed cyclic change in bed friction. Medial moraine patterns are simulated by tracking the englacial and supraglacial trajectory of debris injected at fixed points in the accumulation region. Stratification is assumed to be associated with isochronal surfaces, and vertical foliation is explained in terms of horizontal flattening of strain ellipsoids. Crevasses form when and where the intensity of tensile stress exceeds a prescribed threshold; crack damage is cumulative so that crevasse traces observed at sampling sites are a superposition of the damage accumulated en route. Folding is parameterized but not resolved. By evaluating the deformation gradient tensor along ice particle trajectories and applying the polar decomposition to this tensor, we isolate the cumulative effects of rotation and stretching by ice flow and calculate strain ellipsoids as well as other practical indicators of deformation.

Keypoints:

- Ice dynamics models have sufficient physics to explain many of the structural features of surging and non-surging glaciers.
- Model calculations of the deformation gradient indicate that convergent ice flow favors development of longitudinal foliation structures.
- The propensity for folding can be parameterized using scalar invariants of a rank 3 tensor derived from the deformation gradient.

1. Introduction

For as long as geologists have contemplated glaciers they have sought to explain the structural features of glaciers in terms of their internal processes [e.g., *Agassiz*, 1840; *Forbes*, 1842]. Efforts to test these ideas using numerical ice flow models, following developments in structural geology [*Ramsay*, 1967], are comparatively recent and remain at an early stage [e.g., *Hambrey & Milnes*, 1978; *Hooke & Hudleston*, 1978; *Hubbard & Hubbard*, 2000; *Hambrey et al.*, 2005]. The spatial resolution of glacier flow models limits the scale at which mechanical processes can be resolved and thus the range of processes that can be usefully examined. From the perspective of the generation and evolution of structure, surging glaciers command special attention. Surges can cause large and rapid changes in ice flow rate and internal stresses, potentially amplifying the processes of interest.

This contribution aims to provide a quantitative framework for interpreting a companion paper [*Hambrey & Clarke*, 2019] on the measured and modeled structure of Trapridge Glacier, Yukon, Canada (61° 14′ N, 140° 20′W), a well-studied glacier that from ca. 1980–1999 experienced a slow surge [*Frappé-Sénéclauze & Clarke*, 2007]. Combining field observations and numerical modeling, *Hambrey & Clarke* [2019] analyzed the post-surge structure of Trapridge Glacier including the medial moraine pattern, stratification and foliation, folding, and the density and orientation of crevasse traces. That paper was concerned with the observed structures and the skill of prognostic models to reproduce observations. It avoided the physics and numerics of structure simulation modeling and did not exploit diagnostic models to isolate influences on the formation and transport of structures. In the present paper we test the ability of numerical ice dynamics models to

simulate the processes that produce structures in surging and non-surging glaciers and examine how various forms of flow complexity influence these structures.

We follow the template of Table 1 in *Hambrey & Clarke* (2019) and use standard structural geological notation to label glacier structures: S_0, S_1, etc. for sequential planar structures and F_1, F_2, etc. for successive fold phases. In the present paper we consider primary stratification (S_0), longitudinal foliation (S_1), transverse foliation (S_2), fractures (surface crevassing and crevasse traces) (S_4), recumbent folds (F_3), and medial moraines.

2. Model Overview

Attempts to model the structural evolution of glaciers have mainly focused on strain history [*Hambrey & Milnes*, 1978; *Hooke & Hudleston*, 1978; *Hubbard & Hubbard*, 2000; *Hambrey et al.*, 2005] or on efforts to examine the generation and transport of ice crystal fabric [e.g., *Seddik et al.*, 2011]. Strain history models tend to be based on the calculation of stress and strain-rate ellipsoids and such models are incapable of representing the accumulation of strain. Those approaches are at odds with how structural information is commonly represented by field workers, for example as points projected onto stereographic nets such as Schmidt diagrams and rose diagrams [e.g., *Hubbard & Glasser*, 2005].

The scale at which ice flow velocity components $v_k(x_m, t) = (u, v, w)$ are calculated in a numerical ice dynamics model is set by the cell size of the computational grid. For our flow models we use a Cartesian map grid (Δx=Δy=30 m) with a linearly-stretched vertical axis. Ice temperature is calculated at 11 vertical levels (N_ζ=11) and flow velocity at 21 levels (N_ξ=21). At this resolution, small-scale folding and thrusting are sub-grid processes that cannot be modeled. Furthermore faulting can result in substantial displacements that introduce void space and discontinuous changes in $[u, v, w]$ which are not consistent with

a simple continuum mechanical model. We allow ice cracks to form but represent these as subgrid properties and do not consider the volume change that is associated with crack formation. The model focuses on the extent to which passive transport and rotation during glacier flow can be combined with the accumulated effects of strain and episodic fracture to explain observed patterns of medial moraines, stratification, foliation, folding, and crevasse traces that were identified in a companion paper [*Hambrey & Clarke*, 2019].

The use of vertically-stretched coordinate systems simplifies the numerics but greatly reduces the comprehensibility of the associated mathematical expressions. For this reason we present the model physics in Cartesian coordinates but with the understanding that for numerical analysis the expressions need to be converted to stretched coordinates. A table summarizing the notation for this study can be found at the end of this article. Physical constants and parameter values are listed in Table 1.

2.1. Ice Flow and Surging

Glaciers in the study region are known to have sub-polar thermal regimes [e.g., *Clarke & Blake*, 1991] that can affect both the flow and fracture of ice. Thus we use a thermomechanical numerical ice dynamics model to simulate the evolution of glacier geometry. The flow solver [*Jarosch et al.*, 2013; *Clarke et al.*, 2015] assumes the shallow ice approximation and is supplemented by a temperature solver similar to that of *Greve & Blatter* [2009]. The basic equations of the thermomechanical flow model are

$$\begin{aligned}
\frac{\partial H}{\partial t} &= -\nabla_{xy} \cdot \mathbf{Q} + \dot{b}, \\
\mathbf{Q} &= -\frac{2\mathcal{A}(\rho g)^n}{n+2} \left|\nabla_{xy} S\right|^{n-1} H^{n+2} \nabla_{xy} S + \mathbf{v}_\mathrm{s} H, \\
\mathbf{v}_\mathrm{s} &= -\mathcal{C}(\rho g)^m H^m \left|\nabla_{xy} S\right|^{m-1} \nabla_{xy} S,
\end{aligned}$$

$$\frac{\partial T}{\partial t} = -u\frac{\partial T}{\partial x} - v\frac{\partial T}{\partial y} - w\frac{\partial T}{\partial z} + \frac{1}{\rho c}\frac{\partial}{\partial z}\left(k\frac{\partial T}{\partial z}\right) + \frac{2\mathcal{A}\tau^{n+1}}{\rho c}, \tag{1}$$

where $H =$ ice thickness, $\mathbf{Q} =$ volume discharge of ice per unit width, $\dot{b} =$ ice-equivalent surface mass balance rate, $\mathcal{A} =$ temperature-dependent coefficient in Glen's flow law for ice (*Glen*, 1955), $\rho =$ ice density ($900\,\mathrm{kg\,m^{-3}}$), $g =$ gravity acceleration ($9.80\,\mathrm{m\,s^{-2}}$), $n = 3$ (Glen's flow law exponent), $S =$ surface elevation, $\mathcal{C}(x, y, t) =$ sliding law coefficient, $m = 2$ (sliding law exponent), with constitutive equations: $\mathcal{A} = \mathcal{A}_0 \exp(-E/RT)$ (temperature-dependent creep law coefficient), $k = k_0 \exp(-k_1 T)$ (thermal conductivity), $c = c_0 + c_1 T$ (specific heat capacity), $T_\mathrm{m} = T_0 - \beta(S - z)$ (depth-dependent melting temperature), and physical constants from *Cuffey & Paterson* [2010].

Components of the ice flow velocity field (u, v, w) are reconstructed following a standard approach [*Marshall et al.*, 2000; *Greve & Blatter*, 2009]. As in *Greve & Blatter* [2009], we assume a vertically-stretched coordinate system for both the temperature and velocity fields. For the temperature grid we assume $\zeta_k = [z_k - B(x, y)]/H(x, y)$ and for the velocity grid $\xi_k = [z_k - B(x, y)]/H(x, y)$; both grids are linearly stretched but N_ζ and N_ξ can differ.

Cyclic surging is an important feature of our flow models. Without invoking a surge mechanism we attribute surges to cyclic variations in the basal sliding rate

$$\mathbf{v}_\mathrm{S} = -\mathcal{C}\,(\rho g)^m\, H^m\, |\nabla_{xy} S|^{m-1}\, \nabla S_{xy} \tag{2}$$

caused by cyclic variations in the rate coefficient $\mathcal{C}$ which varies with space and time and takes the limiting values

$$\mathcal{C} = \begin{cases} \mathcal{C}_\mathrm{slide} & \text{normal sliding} \\ \mathcal{C}_\mathrm{surge} & \text{surging.} \end{cases} \tag{3}$$

Spatiotemporal variations in $\mathcal{C}$ are managed by introducing a spatial mask $M(x, y)$ for which $M = 1$ in regions where fast-sliding is possible and $M = 0$ elsewhere; a temporally-

varying mask $M^*(x, y, t)$ with $0 \leq M^* \leq 1$ is obtained from M by introducing a moving boundary $L^*(t)$ that sweeps across the sliding mask M and serves as a shutter that controls the size of the surge activation zone M^* and hence the magnitude of the sliding parameter

$$\mathcal{C}(x, y, t) = \mathcal{C}_{\text{slide}} + [\mathcal{C}_{\text{surge}} - \mathcal{C}_{\text{slide}}] M^*(x, y, t) \tag{4}$$

(Figure 1a). The function $L^*(t)$ is piecewise linear and determines the surge cycle. For a single cycle

$$L^*(t) = \begin{cases} L_{\text{min}} & \text{not surging, } t \leq t_{\text{start}} \\ L_{\text{min}} + \dfrac{t - t_{\text{start}}}{t_{\text{peak}} - t_{\text{start}}} [L_{\text{max}} - L_{\text{min}}] & \text{accelerating phase of surge, } t_{\text{start}} \leq t \leq t_{\text{peak}} \\ L_{\text{peak}} - \dfrac{t - t_{\text{peak}}}{t_{\text{stop}} - t_{\text{peak}}} [L_{\text{peak}} - L_{\text{min}}] & \text{decelerating phase of surge, } t_{\text{peak}} \leq t \leq t_{\text{stop}} \\ L_{\text{min}} & \text{not surging, } t \geq t_{\text{stop}} \end{cases} \tag{5}$$

(Figure 1b). As a final refinement, we smooth the step changes in $\mathcal{C}$ that occur at the upflow and downflow boundaries of the activation zone by applying the smoothing function

$$M^*(x, y, t) = \frac{1}{2} M(x, t) \left\{ \tanh\left[\alpha(L - L_{\text{min}})/\Delta L\right] - \tanh\left[\alpha(L - L^*)/\Delta L\right] \right\} \tag{6}$$

(Figure 1c). In equation 6, we take α=2.5 and ΔL=150 m.

Based roughly on what is known of the surge history for Trapridge Glacier [*Frappé-Sénéclauze & Clarke*, 2007], we take the surge cycle to be 50 years, with a 13-year duration of the active phase and a 37-year quiescent phase. The duration of the accelerating part of the surge phase is 3 years and that of the decelerating phase is 2 years. Surges are initiated in years $1985 \pm 50N$ where N is an integer. Thus, for example, 1945 and 1995 each correspond to year 10 of the surge cycle. We take $\mathcal{C}_{\text{slide}}$=$5 \times 10^{-11}\,\text{m}\,\text{yr}^{-1}\,\text{Pa}^{-2}$ and $\mathcal{C}_{\text{surge}}$=$2.5 \times 10^{-9}\,\text{m}\,\text{yr}^{-1}\,\text{Pa}^{-2}$ which yield reasonable flow rates for the non-surging and surging states.

3. Structure Modeling

The observed structure of Trapridge Glacier [*Hambrey & Clarke*, 2019] provides the motivation for this study. The complexity of that glacier can obscure our understanding of how various structure-forming processes function and how they are influenced by spatial irregularites in bed topography, sliding friction, and surface mass balance and by whether a glacier does or does not surge. We begin by developing a digital elevation model of bed topography that corresponds to a simplified version of Trapridge Glacier which we refer to as "Traplike Glacier". Traplike Glacier flows from west to east and is symmetric about its centerline flow axis. This symmetry is produced by taking the digital elevation model for Trapridge Glacier bed topography $B(x, y)$ (derived from *Flowers & Clarke* [1999] and extended using a simplified version of *Clarke et al.* [2013]) and identifying the central flow axis for Trapridge Glacier (refer to Figure 11 of *Hambrey & Clarke* [2019]), rotating the DEM to align with this axis, resampling the DEM in the rotated grid, and then cropping the new DEM to isolate the Trapridge Glacier catchment. We denote the gridded bed elevation for the new DEM as $B_{i,j}$, where i=1, 2, ..., N_x and j=1, 2, ..., N_y and assume that N_y is an odd number so that j=1 + $(N_y - 1)/2$ corresponds to the j index of the glacier centerline. The smoothed and symmetric bed topography is given by

$$B^*_{i,j} = \frac{1}{2}\left(B_{i,j} + B_{i,N_y+1-j}\right) \tag{7}$$

and taken as the bed topography of the Traplike Glacier reference model (Figure 2). The mass balance forcing $\dot{b}$ is assumed to be elevation-dependent and time-invariant with

$$\dot{b} = \left[\frac{\mathrm{d}\dot{b}}{\mathrm{d}z}\right]_{\mathrm{acc}} \max(S - Z_{\mathrm{ela}}, 0) + \left[\frac{\mathrm{d}\dot{b}}{\mathrm{d}z}\right]_{\mathrm{abl}} \min(S - Z_{\mathrm{ela}}, 0) \tag{8}$$

Z_{ela}=2475 m, $[\mathrm{d}\dot{b}/\mathrm{d}z]_{\mathrm{acc}}$=3.8095 × 10^{-3} yr^{-1}, and $[\mathrm{d}\dot{b}/\mathrm{d}z]_{\mathrm{abl}}$=7.6190 × 10^{-3} yr^{-1}.

Large bedrock bumps complicate the flow of Trapridge Glacier (e.g., *Hambrey and Clarke*, 2019, Fig. 3). By avoiding the full complexity of Trapridge Glacier we can systematically examine how subglacial topography influences ice flow and ice structure. To break the symmetry we can optionally introduce bed bumps (inset Figure 2) centered at various points in the bed (denoted by '+" in Figure 2). Surges occur when a region of reduced bed friction is activated (dashed outline in Figure 2 and equations 4–6).

The Traplike models that we consider are identified as the "reference", "non-surging", "pinched", "bed bump", "balance bump" and "right channel surge" models. The reference model is simplest and has north–south symmetry across its central flowline. The right channel surge model examines the case where the southern half of the glacier experiences cyclic changes in the basal sliding friction while the northern half has constant sliding friction throughout the surge cycle (Figure 2). *Hambrey & Clarke* [2019] suggest that the south channel (i.e., to the south of the medial moraine) shows clearer evidence for surging than the north channel. The simplified model allows the consequences of such a channelization to be explored. The bed bump model examines the effect of bed topography on surges. The north–south symmetry of the reference model is broken by placing bedrock bumps at three points on the bed to create a slalom course for ice flow (Figure 2). The balance bump model assumes the symmetric bed topography of the reference model but breaks symmetry by introducing spatial bumps in the steady mass balance field. These bumps are located at the same spatial positions as the three bumps of the bed bump model and have the same spatial form as the inset of Figure 2. The amplitude of each bump is $\Delta\dot{b}$=+0.60 m yr^{-1} (ice-equivalent). Balance bumps are especially relevant to the

S_0 stratification because they distort the layering. We shall describe the pinched model in a subsequent section.

4. Methods and Algorithms

To compute particle trajectories we employ a one-step two-level scheme in which, for forward tracking, information at time levels t_n and $t_n + \Delta t$ is used to find the position at time step $t_n + \Delta t$ (e.g., *Staniforth & Côté*, 1991). From the point of ice deposition in the accumulation zone $\mathbf{X}_\mathrm{d}$ to the point of emergence in the ablation zone $\mathbf{X}_\mathrm{e}$ the particle follows a trajectory $\mathbf{X}(t)$. The position vector along the trajectory satisfies the equations

$$\frac{\mathrm{d}\mathbf{X}}{\mathrm{d}t} = \mathbf{v}(\mathbf{X}, t) \tag{9}$$

or, equivalently,

$$\frac{\mathrm{d}X_k}{\mathrm{d}t} = v_k(X_m, t). \tag{10}$$

The numerical ice dynamics model calculates the velocity field $\mathbf{v}$ at grid points (x_i, y_j, z_k) and times t_n. For forward (top-down) tracking we approximate equation 10 by

$$X_k(x_m + a_m, t_n + \Delta t) = X_k(x_m, t_n) + v_k(x_m + \frac{a_m}{2}, t_n + \frac{\Delta t}{2})\,\Delta t, \tag{11}$$

which represents a time- and space-centered finite-difference approximation of equation 10 where $a_k = X_k(x_m + a_m, t_n + \Delta t) - X_k(x_m, t_n)$. Solving for a_m by iteration

$$a_k^{p+1} = v_k(x_m + \frac{a_m^p}{2}, t_n + \frac{\Delta t}{2})\,\Delta t \tag{12}$$

and applying these values to equation 11 yields the next down-flow point along the forward particle trajectory.

For backtracking (bottom-up tracking) equation 9 is approximated by

$$X_k(x_m - a_m, t_n - \Delta t) = X_k(x_m, t_n) - v_k(x_m - \frac{a_m}{2}, t_n - \frac{\Delta t}{2})\,\Delta t, \tag{13}$$

and a_m is found by iterating

$$a_k^{p+1} = v_k(x_m - \frac{a_m^p}{2}, t_n - \frac{\Delta t}{2})\,\Delta t. \tag{14}$$

Together, the particle tracking equations allow accurate calculation of the particle trajectories and the possibility of checking integration accuracy by comparing end points for bottom-up and top-down tracking. We find that typical bottom-up vs. top-down spatial and temporal discrepancies seldom exceed 3 cm and 0.05 yr. In rare cases the round-trip closure errors are very large (e.g., with spatial closure errors exceeding 100 m and time closure errors exceeding 10 yr) and the results must be rejected. Such errors indicate a complete failure of the trajectory integration and arise when the starting point for backtracking is at the glacier surface and near the equilibrium line. For this situation the bottom-up and top-down trajectories are very shallow and small errors can cause delayed downward penetration of the bottom-up trajectory or premature emergence of the top-down trajectory.

Round-trip closure errors are not strongly affected by varying the size of Δt or $\Delta\xi$ but this result can be misleading because particle trajectories change somewhat when Δt and $\Delta\xi$ are changed. Comparing the endpoints and emergence times of the bottom-up trajectories among models having different space- and time-step sizes allows the effects of changing these values to be assessed. For example, if both Δt and $\Delta\xi$ are halved (by setting $\Delta t = 0.005$ yr and $N_\xi = 41$) and the results compared with those for the Traplike reference model, the root mean square difference in the emergence positions for a large suite of trajectories is 0.88 m and that of the emergence times is 0.86 yr.

4.1. Semi-Lagrangian Tracers

Numerical modeling of ice particle trajectories in surging glaciers began with the simulation of the isotopic structure of Steele Glacier in Yukon (*Waddington & Clarke*, 1988). Here we use an established semi-Lagrangian approach [*Clarke & Marshall*, 2002; *Clarke et al.*, 2005; *Lhomme et al.*, 2005] to evaluate the modeled ice deposition time $t_\mathrm{d}(x, y, z, t)$ for all englacial points and times. Passive tracers such as t_d and other depositional provenance labels are transported like material particles so the labels are conserved as they move along ice-flow trajectories; thus

$$\frac{\mathrm{d}\Psi}{\mathrm{d}t} = 0, \tag{15}$$

where $\mathrm{d}\Psi/\mathrm{d}t$ denotes a material derivative. Along a trajectory Ψ is constant and it follows that

$$\Psi(x_m, t) = \Psi(x_m - \mathrm{d}x_m, t - \mathrm{d}t) \tag{16}$$

where the points $(x_m - \mathrm{d}x_m, t - \mathrm{d}t)$ and (x_m, t) are on the same flow trajectory. Our model uses small time steps (Δt=0.01 yr) so that equation 16 can be satisfactorily approximated as

$$\Psi(x_m, t) = \Psi\Big(x_m - v_m(x_m, t)\Delta t, t - \Delta t\Big), \tag{17}$$

and higher-order approximations [e.g., *Goelles et al.*, 2014] are unwarranted. (The semi-Lagrangian scheme is explicit, however, so combining a coarse time step (large Δt) with a fine space step (small $\Delta\xi$) can cause integration failure if the Courant–Friedrichs–Lewy (CFL) condition (e.g., *Strang*, 2007) is violated.) By setting Ψ to correspond to the depositional year t_d of an ice particle at the deposition site $[X_\mathrm{d}, Y_\mathrm{,d}, S(X_\mathrm{d}, Y_\mathrm{d}, t_\mathrm{d})]$ one can evaluate $t_\mathrm{d}(x_i, y_j, z_k, t_n)$ for points on the spatial grid at subsequent time steps.

4.2. Characterization of Deformation

A variety of tensors that characterize the rate and magnitude of deformation can be derived from the ice velocity field $\mathbf{v}(x, y, z, t)$. These include the velocity gradient $\mathbf{L} = \operatorname{grad} \mathbf{v}$, strain rate $\mathbf{D} = \frac{1}{2}(\mathbf{L} + \mathbf{L}^T)$ (where $\mathbf{L}^T$ is the matrix transpose of $\mathbf{L}$), and spin $\mathbf{W} = \frac{1}{2}(\mathbf{L} - \mathbf{L}^T)$ which, in subscript notation, can be written as $L_{jk} = \partial v_j/\partial x_k$, $D_{jk} = \frac{1}{2}(L_{jk} + L_{kj})$, and $W_{jk} = \frac{1}{2}(L_{jk} - L_{kj})$. Here and elsewhere in this contribution, we shall move freely between boldface and subscript notation and assume the Einstein summation convention for repeated subscripts in vector and tensor expressions. Subscript notation has the merit of being completely explicit but can sometimes obscure underlying simplicity. For example, the matrix product $\mathbf{AB}$ becomes $A_{ij}B_{jk}$; most computing languages support matrix multiplication, whereas the evaluation of $A_{ij}B_{jk}$ by repeated summation is unnecessarily tortuous.

For glaciological deformations the strains are typically finite and the deformation gradient $\mathbf{F}$ and its polar decomposition are particularly useful. The evolution of $\mathbf{F}$ is obtained by solving the differential equation

$$\frac{\mathrm{d}\mathbf{F}}{\mathrm{d}t} = \mathbf{L}\mathbf{F} \tag{18}$$

[e.g. *Hutter & Jöhnk*, 2004] or, in subscript notation,

$$\frac{\mathrm{d}F_{ij}}{\mathrm{d}t} = L_{ik}F_{kj}. \tag{19}$$

Equation 19 can be integrated using the *McKenzie* [1979] algorithm

$$\mathbf{F}^{n+1} = \mathbf{A}^{-1}\mathbf{B}\mathbf{F}^n, \tag{20}$$

where $\mathbf{A} = \mathbf{I} - \frac{1}{2}\Delta t\,\mathbf{L}$, $\mathbf{B} = \mathbf{I} + \frac{1}{2}\Delta t\,\mathbf{L}$, $\mathbf{I} = \delta_{jk}$ is the identity tensor (Kronecker delta), $\mathbf{A}^{-1}$ denotes the matrix inverse of $\mathbf{A}$, and subscripts $n+1$ and n are time indices. McKenzie

applied this algorithm to a two-dimensional time-independent flow but it also works for three-dimensional time-variable flows. For incompressible flows $\det(\mathbf{F}) = 0$ and this yields a check on the accuracy of the trajectory integrations.

A conceptually simpler approach to evaluating $\mathbf{F}$ that we have not explored is to track individual trajectories of tetrahedral configurations of particles, rather than that of individual particles, and estimate $\mathbf{F}$ by calculating changes in inter-particle distances. If the aim was to evaluate $\mathbf{F}$ at a single downglacier sampling site this could offer a shortcut but several of the structure calculations (for example, the rotation of fracture planes) require $\mathbf{F}$ to be evaluated at selected points along a particle trajectory so, to preserve flexibility, we choose to evaluate and archive $\mathbf{F}$ for every point. For this purpose our method is probably simpler and faster.

The polar decomposition of $\mathbf{F}$ [e.g., *Malvern*, 1969; *Hutter & Jöhnk*, 2004; *Brannon*, 2018]

$$\mathbf{F} = \mathbf{RU} = \mathbf{VR} \tag{21}$$

gives useful information about the deformation: $\mathbf{R}$ is a rigid body rotation and $\mathbf{U}$ and $\mathbf{V}$ are symmetric tensors that represent stretching and from which strain ellipsoids can be calculated. In effect, the polar decomposition presents alternative representations of the total deformation $\mathbf{F}$. Assuming that the initial state is undeformed (i.e., $\mathbf{F}_0 = \mathbf{I}$), the final state $\mathbf{F}$ can be achieved by a non-unique series of deformation steps

$$\mathbf{F} = \mathbf{F}_n \, \mathbf{F}_{n-1} \ldots \mathbf{F}_2 \, \mathbf{F}_1 \, \mathbf{I}. \tag{22}$$

The two-step sequences $\mathbf{F} = \mathbf{RU}$ and $\mathbf{F} = \mathbf{VR}$ represent, respectively, a pure stretch $\mathbf{U}$ followed by a rigid body rotation $\mathbf{R}$ and a rigid body rotation $\mathbf{R}$ followed by a pure stretch $\mathbf{V}$ (where $\mathbf{R}$ is the same for both operations but $\mathbf{U}$ and $\mathbf{V}$ differ).

4.3. Particle Tracking Archive and Post Processing

The thermomechanical ice dynamics model calculates the ice geometry $H(x, y, t)$, temperature $T(x, y, z, t)$, and velocity field $\mathbf{v}(x, y, z, t)$ at every grid point and time step. In principle all these calculations could be archived. However, because of the assumed periodicity of the modeled surges, it is sufficient to archive the results for a single surge cycle. In practice we start the model from an initial ice-free state and run it until it approaches a periodically-repeating state (typically 750–950 years depending on the model). At this time the t_d tracers are introduced and the simulation continues until the elapsed model time is 1150 years. Results of the final 50 years of the simulation are placed in an archive. The particle trajectory calculations and remaining evaluations are performed as post-processing steps. The observation time and spatial locations of surface and englacial sampling sites are defined and back-tracking from these points allows the depositional time and position of the sampled ice to be calculated. Forward tracking from the ice deposition sites to the measurement sites is then performed to confirm the accuracy of the trajectory calculations. During the forward tracking step, the following properties are calculated and archived at each time and location along the trajectories: ice temperature T, ice velocity $\mathbf{v}$, velocity gradient tensor $\mathbf{L}$, strain rate tensor $\mathbf{D}$, eigenvalues and eigenvectors of $\mathbf{D}$, spin tensor $\mathbf{W}$, flow law coefficient $\mathcal{A}$, ice viscosity η, deviatoric stress tensor $\mathbf{s}$, eigenvalues and eigenvectors of $\mathbf{s}$, full stress tensor σ_{jk} (in the hydrostatic approximation), resistive stress $\mathcal{R}_{jk}$, deformation gradient tensor $\mathbf{F}$, rotation tensor $\mathbf{R}$, stretch tensors $\mathbf{U}$ and $\mathbf{V}$,

and the eigenvalues and eigenvectors of **U**. Not all these archived properties are put to use but it seemed prudent to make them available for potential use rather than generate them at some later stage.

Figure 3 shows two simulated particle trajectories for the Traplike reference model. The head and tail of each track are marked by green triangles. Red and blue segments of the trajectories distinguish between parts of the trajectory that are traversed during surges (red) and parts that are traversed during quiescence (blue). Open circles mark decadal times along the trajectories with the farthest downstream markers corresponding to 2000 and the trajectory end points to 2006.6 (the observation year).

The tracks differ both in their length and penetration depth. The map view (Figure 3a) shows that the trajectories start by converging toward the central flow axis then, farther downstream, diverging slightly. The trajectory profiles (Figure 3b) show that the longer track is associated with a greater penetration depth. Here we use the linearly-stretched vertical coordinate $\xi = (z - B)/H$ to avoid graphing complications resulting from the spatially- and temporally-varying ice thickness.

Table 2 is concerned with three points on the long trajectory. Point A represents the starting point, B an intermediate point, and C the end point and sampling site. The location and launch time for the particle at A were chosen so that ice exiting at point C arrives at the pre-determined observation point and observation time 2006.6. Point A was found by backtracking from the known position and time of C. Table 2 gives the calculated start year for A as 1886.99 and the end year as 2006.60; point B corresponds to 1980.00. From the positions and times associated with points A, B, and C, the physical conditions at these points can be calculated using tri-linear interpolation of data extracted from the

flow model archive. For the 0.01 year time step of the flow model and the 119.61 year length of the ABC flow trajectory, there are 11961 evaluations of the various physical properties such as those appearing in Table 2. We do this for all models and trajectories.

4.4. Formation and Transport of Medial Moraines

As for Trapridge Glacier we assume that medial moraine tracks formed by exposed rock debris in the glacier ablation zone were originally deposited at discrete sites in the accumulation zone. Thus the debris trajectories have an englacial component which starts at the surface deposition site and ends where the debris emerges in the glacier ablation zone and a supraglacial component which starts at the point where debris emerges and ends where solid debris is deposited, by surface melting, on an ice-free bed. We assume that englacial debris and material particles of ice move together and that the englacial trajectory is given by the previously introduced solution of the top-down trajectory equation

$$X_k(x_m + a_m, t_n + \Delta t) = X_k(x_m, t_n) + v_k(x_m + \frac{a_m}{2}, t_n + \frac{\Delta t}{2})\,\Delta t. \tag{23}$$

For debris following a supraglacial path the velocity field for debris particles becomes $v_k^{\mathrm{S}}(x, y, t) = v_k[x, y, S(x, y, t), t]$ and the numerical solution is a two-dimensional version of equation 23 with $a_m = (a, b)$ found by iterating

$$\begin{aligned} X_1(x + a^{p+1}, y + b^{p+1}, t_n + \Delta t) &= X_1(x, y, t_n) + v_1^{\mathrm{S}}(x + \frac{a^p}{2}, y + \frac{b^p}{2}, t_n + \frac{\Delta t}{2}) \\ X_2(x + a^{p+1}, y + b^{p+1}, t_n + \Delta t) &= X_2(x, y, t_n) + v_2^{\mathrm{S}}(x + \frac{a^p}{2}, y + \frac{b^p}{2}, t_n + \frac{\Delta t}{2}) \end{aligned} \tag{24}$$

to obtain the solutions

$$\begin{aligned} a &= \Delta t\, v_1^{\mathrm{S}}(x + a, y + b, t_n + \frac{\Delta t}{2}) \\ b &= \Delta t\, v_2^{\mathrm{S}}(x + a, y + b, t_n + \frac{\Delta t}{2}) \end{aligned} \tag{25}$$

which, through equation 23, yields the spatial position of the next supraglacial point on the down-flow trajectory.

Figure 4 shows simulated medial moraine patterns for five different Traplike models viewed at the completion of a surge (cycle year 13 or 1998 for the 1985 surge). For each model there are three debris input points located in the ablation area (marked by colored circles). The equilibrium line altitude (ELA, blue line) is indicated on each plot. Figure 4a is for a non-surging model (obtained by setting $\mathcal{C}_{\text{surge}}$=$\mathcal{C}_{\text{slide}}$ to eliminate fast sliding episodes) and shows the simplest moraine pattern. Figure 4b is for the Traplike reference model and the differences relative to the non-surging model can be attributed to the cyclic flow rate. The oldest (farthest upstream) visible moraine debris dates to around 1950 so only one complete surge cycle is represented in these moraine patterns. The remaining models explore the consequences of breaking the north–south symmetry of the reference model. Figure 4c accomplishes this by introducing bed bumps to the reference model. In Figure 4d the reference bed topography is used and the symmetry is broken by adding bumps to the mass balance field. In Figure 4e the reference bed topography and mass balance are applied but the fast-sliding surging zone is limited to the southern half (right channel) of the glacier (see Figure 4).

Figure 5 shows the time progression of medial moraine patterns that are associated with four of the five models of Figure 4 (the non-surging model has been excluded because the pattern does not change with time). The north–south symmetry of the reference model (Figures 5a1 to 5a5) is maintained throughout the surge cycle and the moraine patterns are quite similar to those for the asymmetrical balance bump model, where symmetry is broken by an asymmetrical mass balance field. The moraine patterns are directly related

to ice dynamics and the effect of balance bumps on ice dynamics is not large. The bed bump model produces highly contorted moraine patterns and the extreme contortions of the right channel surge model produce a surprisingly complex pattern for the northernmost (red line) moraine. This serves as a reminder that the moraine lines are formed by aggregating the distinct trajectories of each debris particle and have no necessary relationship to ice flow trajectories.

4.5. Formation and Transport of the S_0 Stratification

In *Hambrey & Clarke* [2019] the earliest structure to form was identified as primary stratification, labeled S_0 (i.e., formed at the time of surface accumulation) and described as a set of gently dipping layers of coarse bubbly ice separated by diffuse dirty layers. For the model we therefore assume that each of the surfaces that account for the S_0 stratification was formerly subaerial and isochronal; to simulate these surfaces of constant depositional year t_d, we use a semi-Lagrangian tracer transport model (equations 15–17). In nature, temporal variations in the deposition of wind-blown dust, volcanic ash, and the like, account for differences in the delineation of these surfaces.

Figure 6 shows simulations of the S_0 stratification for five Traplike models. The S_0 stratification is associated with the depositional date of surface ice exposed in the ablation zone. In the accumulation zone the depositional date of all surface ice corresponds to the observation year (2000 in these figures). For the non-surging model (Figure 6a) and the reference model (Figure 6b) the S_0 stratification is not complicated and there is little in the patterns that would distinguish a surging from a non-surging glacier. The comparative complexity of the pattern in Figure 6c results from the complex flow produced by surging flow over asymmetrical bed bumps. In contrast the complexity in Figure 6d is caused by

bumps in the surface mass balance field. These perturbations of the mass balance field, though large, do not have a profound influence on the ice velocity field (the glacier margins and medial moraine patterns for the reference model and the balance bumps model are very similar). An important implication is that complexity of the S_0 stratification pattern is not necessarily a reliable indicator of complex flow. Finally, Figure 6e shows the pattern for the right channel surge model. The sharp boundary between surging and non-surging ice produces a dramatic discontinuity in the simulated S_0 horizons.

4.6. Formation and Transport of the S_1 Foliation

On Trapridge and other glaciers, the S_1 foliation is described as longitudinally-oriented, near-vertical, and defined principally by bubble elongation, bubble density, and variations in ice crystal size (layers of fine grained ice alternating with coarse bubbly and coarse clear ice). We shall base our simulations of the formation and transport of S_1 on the deformation gradient tensor F_{jk} found by integrating equation 19 using the *McKenzie* [1979] algorithm. Unlike calculations of $t_d(x, y, z, t)$, which yield isochrons of the S_0 stratification, the deformation gradient is only available at points along ice flow trajectories. Thus producing a surface map of S_1 at grid points (x_i, y_j) entails back-tracking the trajectories for each of these points of interest, then performing forward integrations of $\mathbf{F}$ along the trajectory. There is no semi-Lagrangian alternative that might simplify this task. Because particle tracking is computationally intensive, we limit our efforts to a grid of 61 surface observation sites (Figure 7). We proceed by back-tracking from these measurement sites (x_s, y_s, z_s) and measurement times t_s to their up-glacier depositional sites (x_d, y_d, z_d) and deposition times t_d. Here, the vertical coordinates z_s and z_d correspond to z_s=$S(x_s, y_s, t_s)$ and z_d=$S(x_d, y_d, t_d)$ from the ice dynamics model. Having found these points, we com-

mence forward-tracking from $(x_\mathrm{d}, y_\mathrm{d}, z_\mathrm{d}, t_\mathrm{d})$ to $(x_\mathrm{s}, y_\mathrm{s}, z_\mathrm{s}, t_\mathrm{s})$ and perform the trajectory integrations that yield $F_{jk}(x_\mathrm{s}, y_\mathrm{s}, z_\mathrm{s}, t_\mathrm{s})$, the total strain at the measurement site.

The deformation gradient tensor carries information about the strain ellipsoid, which is the focus of our interest in the S_1 foliation. The polar decomposition $\mathbf{F} = \mathbf{RU} = \mathbf{VR}$ decomposes $\mathbf{F}$ into a stretch $\mathbf{U}$ followed by a rotation $\mathbf{R}$ or, alternatively, a rotation $\mathbf{R}$ followed by a stretch $\mathbf{V}$. The rotation is the same for both cases but the stretch tensors $\mathbf{U}$ and $\mathbf{V}$ differ; they have identical eigenvalues but differing eigenvectors. The stretch tensors $\mathbf{U}$ and $\mathbf{V}$ are symmetric with identical eigenvalues $\lambda_1^\mathbf{U}$, $\lambda_2^\mathbf{U}$, and $\lambda_3^\mathbf{U}$ that correspond to the principal semi-axis lengths of the strain ellipsoid. The eigenvectors of $\mathbf{U}$, written $\mathbf{N}_1^\mathbf{U}$, $\mathbf{N}_2^\mathbf{U}$, and $\mathbf{N}_3^\mathbf{U}$, are mutually orthogonal but have no particular orientation relative to the (x, y, z) coordinate system of the ice dynamics model. The eigenvalues and their associated eigenvectors are ordered so that $\lambda_1^\mathbf{U} \geq \lambda_2^\mathbf{U} \geq \lambda_3^\mathbf{U}$ and the eigenvectors form the basis vectors for a right-handed coordinate system. The S_1 foliation is assumed to coincide with the plane formed by the maximum and intermediate eigenvalues of $\mathbf{U}$, i.e., $\mathbf{N}_1^\mathbf{U}$ and $\mathbf{N}_2^\mathbf{U}$; the eigenvector $\mathbf{N}_3^\mathbf{U}$ is perpendicular to this plane. It remains to apply the rotation $\mathbf{R}$ and place these vectors in their final configuration: $\mathbf{RN}_1^\mathbf{U}$, $\mathbf{RN}_2^\mathbf{U}$, and $\mathbf{RN}_3^\mathbf{U}$. However this is needlessly circuitous because the eigenvectors of $\mathbf{V}$ yield the same information directly because $\mathbf{N}_1^\mathbf{V} = \mathbf{RN}_1^\mathbf{U}$, $\mathbf{N}_2^\mathbf{V} = \mathbf{RN}_2^\mathbf{U}$, and $\mathbf{N}_2^\mathbf{V} = \mathbf{RN}_2^\mathbf{U}$.

The unit vector $\mathbf{N}_3^\mathbf{V}$ is normal to the plane of the S_1 foliation. As in Figure 6 of *Hambrey & Clarke* [2019], this vector can be mapped as a point on a lower hemisphere stereographic projection by choosing the sense of $\mathbf{N}_3^\mathbf{V}$ to be downward-pointing. Thus, for example, if (x_p, y_p, z_p) are components of the unit vector $\mathbf{N}_3^\mathbf{V}$ and z_p is positive, the sense is reversed

by setting $\mathbf{N_3^V}$=$-(x_p, y_p, z_p)$. The plunge angle of $\mathbf{N_3^V}$ is φ_3=arctan$(z_p/\sqrt{x_p^2 + y_p^2})$ and the dip of the plane normal to $\mathbf{N_3^V}$ is δ_3=$\pi/2-\varphi_3$ (in radians).

Alone, the orientation of the $\mathbf{N_3^V}$ plane says nothing about the strength of the foliation that is associated with it. It is reasonable to assume that the geometry of strain ellipsoids influences foliation development but the processes that connect ice strain and ice foliation merit future study. For Trapridge Glacier the S_1 foliation was attributed to enhanced ablation of ice that contained a high density of elongated bubbles. Bubbles have been taken as strain indicators although diffusion processes can complicate this idea [e.g., *Alley & Fitzpatrick*, 1999; *Gay*, 1968; *Hudleston*, 1977; *Nakawo & Wakahama*, 1981]. Our association of the S_1 foliation with the geometry and orientation of strain ellipsoids is contingent on the extent to which the geometry of strain ellipsoids influences the geometry of bubbles and the orientation of ice fabric. For the present study we assume that the following ellipsoid properties favor development of the S_1 foliation: the dip angle δ_3 of the $\mathbf{N_3^V}$ eigenvector cannot be small ($\delta_3 > 30°$) and the axis ratio $\kappa_{2:3}$=$\lambda_2^{\mathbf{U}}/\lambda_3^{\mathbf{U}}$ must be large enough to significantly flatten the ellipsoid ($\kappa_{2:3} > 5$). We suspect that a small axis ratio $\kappa_{1:2}$=$\lambda_1^{\mathbf{U}}/\lambda_2^{\mathbf{U}}$ (yielding a disk-like ellipsoid rather than a blade-like one) is also favorable but do not apply this restriction.

Figure 8a shows simulation results for the Traplike reference model presented in the form of equal-area lower-hemisphere stereographic projections of the poles of the $\mathbf{N_3^V}$ eigenvector in the form of a scatterplot (left) and contoured density plot (right) of the same data. Most of the 61 plotted points fail one or both of the criteria that we consider favorable for the S_1 foliation. For yellow points: $\delta_3 < 30°$; for green points: $\kappa_{2:3} < 5$; red points fail both tests. These exclusion criteria would not eliminate steeply-dipping

transverse features if such existed. Figure 8b shows stereoplots for data that has been "edited" to remove the excluded points. Figure 8c shows the site locations and uses the same color coding. The accepted points unquestionably correspond to a steeply dipping longitudinal foliation, defining characteristics of S_1, but there are too few points to yield a pleasing contour plot. For additional insight, Table 3 summarizes the calculated ellipsoid properties and results of exclusion tests for selected points plotted in Figures 8a and 8c.

In contrast to Figure 8, the Trapridge Glacier simulation [*Hambrey & Clarke*, 2019, Fig. 17] yielded 45 (of 121) suitable points. We speculate that the channel geometry for the Traplike reference model does not favor development of the S_1 foliation. Previous publications on this foliation, including *Hambrey & Clarke* [2019], have called attention to the association of the S_1 with converging flow. For example, the conspicuous "longitudinal septum" of Blue Glacier (Washington State) appears to form at the confluence of ice flowing from north and south basins of that glacier [*Allen et al.*, 1960], and White Glacier (Axel Heiberg Island) has a wide accumulation area feeding a long, straight, and narrow tongue [*Hambrey & Müller*, 1978], as does Midtre Lovénbreen (Svalbard) [*Hambrey et al.*, 2005]. To assess these interpretations we modified the bed topography of the reference model to obtain a channel that would favor convergence of ice flow toward the central flow axis. This was accomplished by smoothly distorting the DEM of bedrock topography (Figure 2) so that the north–south symmetry was preserved but the channel width was narrowed. In the map coordinate system of Figure 2, the zone of progressive narrowing is 1170 E–1920 E, with a maximum narrowing at 1920 m; between 1920 E–2670 E the constricted channel progressively widens. Upstream from 1170 E and downstream from 2670 E the DEM is identical to that for the reference model. These zones of narrowing

and widening are indicated on the site map (Figure 8c1). We reasoned that the flow convergence introduced by modifying the channel geometry would favor increased flattening of the strain ellipsoids and thus promote development of the S_1 foliation. We call this modification of the Traplike reference model the "pinched" model.

Figures 8a1 to 8c1 show the simulation results for the Traplike pinched model. Of the 61 points examined in the pinched model, 19 pass the exclusion criteria and the resulting edited plots (Figure 8b1) correspond to a steeply dipping longitudinal foliation. Comparison of the site map for the pinched model and the reference model clearly indicates that flow convergence leads to significant increases in ellipsoid flattening and thus to significant enhancement of S_1.

Figure 9 presents the results of efforts to simulate the S_1 foliation for four Traplike Glacier models and as many as 61 surface sites (Figure 9). The stereographic projection for the reference model (Figure 9a) and the no-surge model (Figure 9b) are closely similar and indicate a strongly developed near-vertical S_1 foliation that is aligned with the ice flow direction. These points break the predominant north–south symmetry of Figures 9a and 9b and complicate the contour plots. A closer study reveals that the discordant points seem to be associated with compressive flow which under some circumstances can cause the minor axis of the ellipsoids to be aligned with the ice flow direction and the plane of $\mathbf{N}_1^{\mathbf{V}}$ and $\mathbf{N}_2^{\mathbf{V}}$ to be sub-horizontal.

By focusing attention on the geometry of strain ellipsoids we have blurred the distinction between ellipsoids and foliations. For Trapridge Glacier, *Hambrey & Clarke* [2019] noted that the S_1 foliation is defined principally by crystal size, bubble elongation, and bubble density and associated variations in surface ablation rate. If the ice and bubbles experience

and preserve the same strain history then it seems reasonable to expect that horizontally flattened disk-like bubbles would intersect the melting ice surface more frequently than the same number density of spheroidal bubbles and melt penetration would be enhanced. In this case it is likely that our requirement that $\kappa_{2:3}<5$ is too stringent.

In the course of this examination of the S_1 foliation, we remained open to the possibility that examples of the S_2 transverse foliation identified in *Hambrey & Clarke* [2019] might be generated by the same processes that produced discordant points that do not match the observed longitudinal foliation in Figures 9a to 9d. However strain ellipsoid simulations do not support this hypothesis and the interpretation that the S_2 foliation originally formed as crevasse traces seems to be the correct one. We return to this discussion following the sections on crevasse traces and crack density.

4.7. Formation and Transport of Folded Ice

Our model does not attempt to resolve the intricate strain that can result from recumbent englacial folding (F_3 in *Hambrey & Clarke* [2019]). Instead we propose a simple scalar parameterization that aims to identify strain conditions that favor folding. First, we seek a tensor that contains the desired information and then examine its scalar invariants which, like the tensor, are independent of the coordinate system. Tensors such as **L**, **D**, and **W** are not useful because they involve rates of deformation rather than the time-integrated consequences. The deformation gradient **F** has the merit of quantifying the accumulated strain but is nonetheless unsatisfactory because the deformations that it can characterize are insufficiently complex to produce folding.

We therefore focus on the gradient of the deformation gradient **F** which we write as $\mathbf{T} = \mathrm{grad}(\mathbf{F})$. **T** is a rank three tensor ($T_{ijk} = \partial_i F_{jk}$ in subscript notation) which has

12 scalar invariants [*Ahmad*, 2011]. One of these invariants is linear $\mathcal{L} = \epsilon_{ijk}T_{ijk}$ where ϵ_{ijk} is the alternating tensor [e.g., *Malvern*, 1969, p. 21]; the remaining invariants are quadratic, for example, $\mathcal{Q}_1 = T_{iik}T_{ppk}$ and $\mathcal{Q}_{11} = \frac{1}{2}(T_{ijk}T_{kij} + T_{ijk}T_{jki})$. By inspection and numerical experiments we find that the quadratic invariants $\mathcal{Q}_2 = T_{iji}T_{pjp}$, $\mathcal{Q}_4 = T_{ijk}T_{ijk}$, and $\mathcal{Q}_7 = T_{ijk}T_{kji}$ are useful indicators of deformation fields that favor folding. Results are similar for each of the three invariants and have comparable scaling so there is no clear basis for preferring one over another. We take

$$\mathcal{Q}_2 = (T_{111} + T_{212} + T_{313})^2 + (T_{121} + T_{222} + T_{323})^2 + (T_{131} + T_{232} + T_{333})^2 \tag{26}$$

as our scalar folding parameter. Additional features of $\mathcal{Q}_2$ are that it is non-negative, increases when conditions favor folding, and decreases when conditions favor unfolding.

Evaluating $T_{ijk} = \partial_i F_{jk}$ is not straightforward and we extend the scheme of *McKenzie* [1979] as follows: we note that T_{1jk}, T_{2jk} and T_{3jk} are rank two tensors, then we differentiate (19)

$$\frac{\partial}{\partial x_1}\frac{\mathrm{d}F_{ij}}{\mathrm{d}t} = \frac{\partial}{\partial x_1}L_{ik}F_{kj} = \frac{\partial L_{ik}}{\partial x_1}F_{kj} + L_{ik}\frac{\partial F_{kj}}{\partial x_1} \tag{27}$$

to get

$$\frac{\partial}{\partial x_1}\frac{\mathrm{d}\mathbf{F}}{\mathrm{d}t} = \frac{\partial \mathbf{L}}{\partial x_1}\mathbf{F} + \mathbf{L}\frac{\partial \mathbf{F}}{\partial x_1}. \tag{28}$$

An algorithm for integrating equation 28 can be obtained by taking derivatives of equation 20, for example,

$$\frac{\partial \mathbf{F}^{n+1}}{\partial x_1} = \frac{\partial \mathbf{A}^{-1}}{\partial x_1}\mathbf{B}\mathbf{F}^n + \mathbf{A}^{-1}\frac{\partial \mathbf{B}}{\partial x_1}\mathbf{F}^n + \mathbf{A}^{-1}\mathbf{B}\frac{\partial \mathbf{F}^n}{\partial x_1}, \tag{29}$$

and similarly for x_2 and x_3. Finally, the results of the three integrations can be assembled to form $\mathbf{T}^{n+1} = \mathrm{grad}(\mathbf{F}^{n+1})$.

Figure 10 shows the results of efforts to model the propensity for folding along centerline profiles (Figure 7) for the non-surging, reference, and bed bump Traplike Glacier models. The contoured variable is $\log_{10} \mathcal{Q}_2$ where $\mathcal{Q}_2$ is the folding parameter. Large positive values of $\log_{10} \mathcal{Q}_2$ (warm colors) indicate deformations that are conducive to folding and large negative values the opposite. The procedure for evaluating $\mathcal{Q}_2$ at t_{obs} is not straightforward. First, a vertical centerline grid is defined and an observation year chosen. This yields an array of grid points (x_i, z_k) at time $t{=}t_{\text{obs}}$. In this application the backtracking involves englacial as well as supraglacial sites. Points near the bed or the glacier terminus are challenging to backtrack accurately and points far up-glacier have a short strain history and are unlikely to experience appreciable folding. Thus we omit the bottom-most layer from the plot as well as points in the accumulation zone and near the glacier terminus.

Comparison of the plotted results for the non-surging, reference, and bed bump models (Figure 10) does not reveal striking differences among the models. Warm colors correspond to regions where folds are most likely to be located and cool colors to highly-unfavorable regions; the color scales for each panel are identical. In every case, folds are concentrated near the glacier bed, especially near bedrock topography, and with an increasing trend toward the glacier terminus. Near the terminus the thickness of the folding zone increases. The plotted profiles suggest that the non-surging model is most conducive to folding, as was also the case for the non-surging Trapridge Glacier model [*Hambrey & Clarke*, 2019, Fig. 18]. This might be explained because creep deformation is greatest for non-surging models and we cannot simulate thrusting, which would surely be an important process for

fold generation in surging glaciers. We do not regard the results of our fold simulations to be authoritative.

4.8. Formation and Transport of Crevasse Traces

Modeling the formation and transport of crevasse traces proved to be challenging. Judging from comparisons of observed and modeled crevasse trace records for Trapridge Glacier [*Hambrey & Clarke*, 2019] much more work will be needed to achieve success. The heart of the problem is that glacier flow models rely on a non-linear viscous flow law and for such materials, fractures cannot occur. What follows is based on how fracture processes and viscous flow are reconciled using the linear elastic fracture mechanics (LEFM) model. Although, in glaciology, the LEFM is strongly associated with *van der Veen* [1999, 2007] and the crack model he advocates, the essential features of the LEFM are that viscous stresses are treated as elastic stresses and that cracking occurs when some stress threshold is exceeded.

4.8.1. Ice Fracture Model

We postulate that the cracks tend to form during the active phase of surges and are caused by tensile stresses in the ice. At the time of their formation the normal vector to crack planes is assumed to be coaligned with the principal axis of tension, as for Mode I cracks. To quantify these ideas we first evaluate components of the deformation rate tensor D_{jk} from the modeled velocity field $v_j(x_m, t)$. The corresponding deviatoric stress is taken to be

$$s_{jk} = 2\eta D_{jk}, \tag{30}$$

where η is the effective viscosity and

$$\frac{1}{\eta} = \frac{1}{\eta_0} + 2\mathcal{A}\tau^{n-1}, \tag{31}$$

where $\eta_0 = 10^{15}$ Pa s is the residual viscosity; $\tau = \frac{1}{2}\left(s_{jk}s_{kj}\right)^{\frac{1}{2}}$ is the effective stress. The full stress tensor σ_{jk} can be calculated from the deviatoric stress tensor using the following approximations from *Greve & Blatter* [2009]:

$$\sigma_{11} = 2s_{11} + s_{22} - \rho g(S - z) \tag{32}$$

$$\sigma_{22} = 2s_{22} + s_{11} - \rho g(S - z) \tag{33}$$

$$\sigma_{33} = -\rho g(S - z), \tag{34}$$

with σ_{12}=σ_{21}=s_{12}, σ_{13}=σ_{31}=s_{13}, and σ_{23}=σ_{32}=s_{23}. The full stress tensor can be expressed in terms of its principal components, the eigenvalues of σ_{jk},

$$\sigma_{jk} = \begin{bmatrix} \sigma_1 & 0 & 0 \\ 0 & \sigma_2 & 0 \\ 0 & 0 & \sigma_3 \end{bmatrix}, \tag{35}$$

where $\sigma_1 \geq \sigma_2 \geq \sigma_3$ and the associated eigenvectors $\mathbf{N}^\sigma = [N_x^{\sigma_1}, N_y^{\sigma_2}, N_z^{\sigma_3}]$, etc., are unit vectors that form the columns of the matrix

$$N_{jk}^\sigma = \begin{bmatrix} N_x^{\sigma_1} & N_x^{\sigma_2} & N_x^{\sigma_3} \\ N_y^{\sigma_1} & N_y^{\sigma_2} & N_y^{\sigma_3} \\ N_z^{\sigma_1} & N_z^{\sigma_2} & N_z^{\sigma_3} \end{bmatrix}. \tag{36}$$

We assume that crevasse traces are the healed record of Mode I cracks formed as ice moves through the glacier. At the time of formation, the crack plane is near-vertical and oriented so that the outward normal to the crack plane is orthogonal to the direction of maximum tensile stress. We experimented with both the *Nye* [1957] and *van der Veen* [1999] crack criteria and prefer the Nye model for our purposes. From equation 32, a rotation about the z axis allows the maximum stress to be written, giving

$$\sigma_1 = 2s_1 - \rho g(S - z) \tag{37}$$

where s_1 is the maximum principal value of the deviatoric stress tensor s_{jk} and $s_2 = 0$. Nye's condition is simply that $\sigma_1 > 0$, i.e., the maximum stress must be tensile.

In the model, as in nature, cracks form episodically along the flow trajectory $[X_\mathrm{p}(t), Y_\mathrm{p}(t), Z_\mathrm{p}(t)]$ in response to spatially- and temporally-changing stresses so that parcels of ice accumulate crack damage en route to downglacier sampling sites. We assume that all cracks are Mode I and are initially oriented so the crack plane is vertical and the normal vector to the crack plane is aligned with the direction of the maximum tensile stress σ_1 (equation 37). At the time of formation t_p of an individual crack at $(X_\mathrm{p}, Y_\mathrm{p}, Z_\mathrm{p})$ the crack plane has the unit normal vector $[n_\mathrm{p}]_j = N_j^{\sigma_1}(X_\mathrm{p}, Y_\mathrm{p}, Z_\mathrm{p}, t_\mathrm{p})$ where $N_j^{\sigma_1} = \mathbf{N}^{\sigma_1}$ is the eigenvector associated with the maximum principal stress σ_1 (i.e., the direction of maximum tensile stress). For the crack event at $(X_\mathrm{p}, Y_\mathrm{p}, Z_\mathrm{p}, t_\mathrm{p})$ the deformation gradient is $\mathbf{F}(X_\mathrm{p}, Y_\mathrm{p}, Z_\mathrm{p}, t_\mathrm{p})$ and polar decomposition gives the cumulative rotation from the deposition point to the crack point as $\mathbf{R}(X_\mathrm{p}, Y_\mathrm{p}, Z_\mathrm{p}, t_\mathrm{p})$. Subsequent to the crack event the ice particle is transported downflow to an observation site $(X_\mathrm{s}, Y_\mathrm{s}, Z_\mathrm{s})$ at time t_s. The cumulative rotation from the point of deposition $(X_\mathrm{d}, Y_\mathrm{d}, Z_\mathrm{d})$ at time t_d to the point and time of observation is $\mathbf{R}(X_\mathrm{s}, Y_\mathrm{s}, Z_\mathrm{s}, t_\mathrm{s})$ (calculated from $\mathbf{F}(X_\mathrm{s}, Y_\mathrm{s}, Z_\mathrm{s}, t_\mathrm{s})$) and rotation of the crack plane from the point and time of crack formation to the point and time of observation is found from $\mathbf{R}_\mathrm{s} = \mathbf{R}_{\mathrm{p}\to\mathrm{s}}\mathbf{R}_\mathrm{p}$

$$\mathbf{R}_{\mathrm{p}\to\mathrm{s}} = \mathbf{R}_\mathrm{s}\mathbf{R}_\mathrm{p}^{-1}. \tag{38}$$

Equation 38 can be applied to the outward normal unit vectors for each of the crack planes $\mathbf{n}_\mathrm{p}$ to determine the amount of rotation each crack experiences between its place and time of origin and its point and time of exhumation at a sampling site

$$\mathbf{n}_{\mathrm{p}\to\mathrm{s}} = \mathbf{R}_{\mathrm{p}\to\mathrm{s}}\mathbf{n}_\mathrm{p}. \tag{39}$$

4.8.2. Blanking Model

The LEFM model is capable of predicting when conditions are favorable for crack formation but neglects important physics. Ice fracture is accompanied by stress release and modification of the stress field, whereas the LEFM model is most useful in describing the behavior of undamaged material. The occurrence of a crack at some point (x_p, y_p, z_p) and time t_p prevents or inhibits the occurrence of a new crack at a nearby point and time. Over time, cracks can close and anneal so that ice can recover its former strength, allowing the possibility of a new crack if stress conditions are favorable. All this is beyond the reach of the LEFM and viscous flow models such as those based on Glen's creep law. For these models (ours is one of them), stress conditions that cause a crack at point (x_p, y_p, z_p) and time t_p continue to prevail after a crack has formed; thus there is nothing to prevent the occurrence of cracks at subsequent times $t_p + \Delta t$, $t_p + 2\Delta t$, etc. As a remedy, we turn to a rule-based approach and propose that the occurrence of a crack at (x_p, y_p, z_p, t_p) prevents the occurrence of a fresh crack at that site until one of the following conditions is satisfied: (1) a healing time $\tau_\star$ has elapsed so that $t \geq t_p + \tau_\star$; (2) the cracked-damaged ice has traveled a distance $\Delta s_\star$ from the crack-formation site so that $(x-x_p)^2+(y-y_p)^2+(z-z_p)^2 > \Delta s_\star^2$ or, equivalently, $(u_p^2+v_p^2+w_p^2)(t-t_p)^2 > \Delta s_\star^2$ where (u_p, v_p, w_p) are scalar components of $\mathbf{v}_p$. For the present work and that of *Hambrey & Clarke* [2019] we take $\tau_\star$=0.5 yr and $\Delta s_\star$=2.5 m. We refer to this procedure as "blanking" because it is rule-based, motivated by the wish to limit the number of modeled crack events, and only loosely connected to ice physics.

4.8.3. Other Considerations

In Figures 8 and 17 of *Hambrey & Clarke* [2019] the Schmidt diagrams (equal-area, lower hemisphere projections) are based on roughly 50 samples for each site. In the present paper and for the modeled cracks in *Hambrey & Clarke* [2019], the number of counted cracks, though limited by the blanking rule, commonly exceeds N=50 and we must select 50 from this larger collection in order to maintain consistency with the Trapridge Glacier field study [*Hambrey & Clarke*, 2019]. We do this by randomly choosing 50 events from those identified, using a random number generator to ensure objectivity.

A second consideration is that modeled crevasse traces differ from the observed traces in an important way. Unlike modeled crevasse traces, those observed in the field at a given time t_s are not concentrated at a single site (x_s, y_s, z_s) but separately identified in a patch of ice that surrounds the sampling site. Thus, for field measurements, the observed ice constitutes a "parcel" whereas for the model it is a single point. This difference has implications for observation vs. model comparisons. There is nothing in the field procedure to prevent two cracks from having identical orientations thus we do not purge near-duplicates from the field data or from the modeled traces. Crack history is recorded in different ways in the glacier and the model. The model treats the crack history as a palimpsest of cracks applied to a single material point as it migrates through the glacier. Whereas in the field situation the observed cracks are located at different, though nearby, points and then aggregated to produce a stereoplot that supposedly represents the cracks at a site. In reality a single particle of ice is not subjected to a multiplicity of cracking events.

4.8.4. Modeled Crevasse Trace Orientations

Figure 11 presents the simulated orientation of surface cracks at 21 sites for the Traplike reference model observed in 2006.6 (year 21.6 of the surge cycle). The modeled 2006.6 ice flow direction at each measurement site is indicated by arrow annotations. The modeled flow has perfect north–south symmetry and this is reflected in the north–south symmetry of the stereo- and rose plots (e.g., E1S1 and E1N1). The slight asymmetry in the point scatter and contour plots, most obvious for the centerline sites (E1C, E2C, EC3), results from random selection of the plotted points (section 4.8.3) and, for the rose plots, because the boundaries for rose segment bins lack north–south symmetry (e.g., 0–10°, 10–20°, relative to East)

For centerline sites, cracks are oriented transverse and parallel to the eastward ice flow direction and remain near-vertical along the track. Post-crack rotation is slight and confined to the vertical plane. The contrast between centerline sites and S1 (southline) sites is striking, despite the small (90 m) separation of these lines. The cause of the surprising complexity of the simulated crack patterns cannot be inferred from close study of these plots and can only be clarified by examination of the ice particle trajectories (as for Figure 3b), with special attention to the orientation and timing of crack formation. For example, the simplicity of the patterns for E3S1 compared to those for E2S1 appears to relate to the fact that ice at E3S1 experienced only three major episodes of mainly-transverse cracking whereas, despite its shorter trajectory, ice at E2S1 experienced four main cracking episodes and the crack orientation at the time of formation was variably, transverse, longitudinal, and diagonal. Another consideration is that long trajectories tend to have greater depth penetration than short trajectories, allowing ice to descend below the maximum depth of crevasses and avoid cracking.

Figure 12 gives the modeled orientation of crevasse traces for the Traplike bed bump model. The topographical asymmetry is reflected in the asymmetry of the stereographic and rose plots but the increased complexity of the bed topography and ice flow does not appear to result in greater complexity of the crack orientation plots.

4.8.5. Modeled Crack Counts

The analysis of crack counts and the classification of crevasse traces as transverse, diagonal, or longitudinal, is intended to complement the similar analysis [*Hambrey & Clarke*, 2019] of Trapridge Glacier data. For this analysis we count all cracks produced by a model and culled by a blanking rule (hence no random selection is performed). Crack orientations relative to the ice flow direction $\Delta\vartheta = |\vartheta_{\text{crack}} - \vartheta_{\text{flow}}|$ at the time of observation (2006.6 or year 21.6 of the modeled surge cycle) are classified as diagonal ($\Delta\vartheta$=20−70°), longitudinal ($\Delta\vartheta$=70−90°), or transverse ($\Delta\vartheta$=0−20°). The foregoing specifications are the same as those used in *Hambrey & Clarke* [2019].

Figure 13 shows the crack count and orientation for surface cracks at 21 sites observed at 2006.6 (year 21.6 of the modeled surge cycle). Figures 13a and 13b are for the no-surge and reference model; both show the expected north-south symmetry relative to the central flow axis. Interestingly, there is little difference in the crack count for the non-surging and surging cases. The greatest difference is that for the E1 line (farthest upglacier) where there is a substantially higher crack count for the reference (surging) glacier. For a non-surging glacier the region near the ELA is not subjected to large tensile stresses so this could explain the discrepancy. For the E3 line (farthest downglacier), the non-surging model yields a substantially higher proportion of longitudinal cracks than the reference

(surging) model. Figures 13c and 13d are for the bed bump and right channel surge models.

One of the intriguing results for Trapridge Glacier (*Hambrey & Clarke*, 2019, Fig. 20) was the observation that the maximum crack count was recorded at an up-glacier site, contradicting the intuitive idea that the oldest ice would experience the greatest crack damage. The crack counts for the reference model and non-surging model (Figures 13a and 13b) show a similar tendency, although for the surging model the feature is less pronounced than for the observed and modeled counts for Trapridge Glacier. For the reference, bed bump, and right channel surge models (all of which surge) longitudinal crevasses are the least common whereas they are abundant in the non-surging model.

4.8.6. Possible Crack Origin for the S_2 Foliation

In *Hambrey & Clarke* [2019] the S_2 foliation was described as a transverse foliation having a 30–50° up-glacier dip and interpreted as a structure originally formed as near-vertical transverse crevasse traces that were subsequently compressed and rotated. Here we examine this interpretration from a modeling perspective. Figure 14 illustrates the simulated compression and rotation of transverse cracks as they approach the glacier terminus. We choose the Traplike reference model to remove distractions such as asymmetric bed topography and choose centerline (E3C–E5C) and southline (E3S1–E5S1) sites to minimize flow complexity. Figure 14a shows the site locations and Figures 14b and 14c the corresponding stereographic projections for the simulated crack planes. For up-glacier sites along the centerline (E3C and E3.5C) the crack planes are transverse to flow, mutually parallel, and near-vertical. At site E4C the verticality and parallelism of the crack planes start to diverge, a few planes dip slightly down-glacier but the majority dip up-glacier

with dips in the 80–90° range. The tendency for rotation and spreading of the crack planes continues with sites E4.5C and E5C having a dip range of 20–90°.

The picture is more complicated for the southline sites but leads to the same general conclusion. For sites E3S1–E4S1 the majority of simulated cracks, though broadly transverse to flow, are near-vertical with slight up-glacier dips that lie well outside of the observed 30–50° dip range. At site E4.5S1, the crack distribution changes abruptly with the appearance of a cluster of non-vertical cracks that are transverse to flow and have moderate (30–50°) up-glacier dip angles. A second cluster of points, representing near-vertical cracks dipping upglacier but southward, also appears. At site E5S1, nearest the terminus, the pattern simplifies to a single cluster of points corresponding to sets of transverse cracks dipping upglacier at moderate angles. To interpret this complicated site-to-site variation it is important to recognize that the ice emerging at each site follows completely different pathways; differences between adjacent sites cannot be attributed to changes that occur while ice moves from one site to the next. (In fact ice does not move from one site to the next since; it melts where it emerges.) The longest and deepest penetrating flow trajectories emerge near the glacier terminus and parcels of this ice can experience substantial flow rotation, in a vertical plane, caused by frictional interaction with the glacier bed. In contrast, ice emerging farther up-glacier may follow a shallower trajectory and have little frictional interaction with bed but might experience horizontal shearing and rotation from interaction with channel sidewalls.

To shed light on the magnitude of the cumulative rotation of ice parcels at measurement sites, Table 4 summarizes information on the total rotation experienced by ice at the centerline and southline sites. The calculations are based on the rotation tensor $\mathbf{R}$, computed

from the polar decomposition of $\mathbf{F}$, where $\mathbf{R}$ corresponds to the cumulative rigid-body rotation. To illustrate the procedure we consider the tutorial example presented in section 4.3. The values of the rotation tensor along trajectory ABC in Figure 3) are tabulated in Table 4. At the start (A) and endpoint (C) of the trajectory

$$\mathbf{R}_{\mathrm{A}} = \begin{bmatrix} 1 & 0 & 0 \\ 0 & 1 & 0 \\ 0 & 0 & 1 \end{bmatrix} \tag{40}$$

and

$$\mathbf{R}_{\mathrm{C}} = \begin{bmatrix} 0.207 & -0.965 & 0.160 \\ 0.972 & 0.185 & -0.146 \\ 0.111 & 0.186 & 0.976 \end{bmatrix}. \tag{41}$$

Columns of $\mathbf{R}$ correspond to unit vectors that are embedded in and transported with an ice parcel and which form a Cartesian coordinate system. Thus for $\mathbf{R}_{\mathrm{A}}$ these vectors are $[1, 0, 0]$, $[0, 1, 0]$, and $[0, 0, 1]$, corresponding to an (x, y, z) system that is aligned with geographical East, North, and the zenith. For $\mathbf{R}_{\mathrm{C}}$ these vectors have rotated to $[0.207, 0.972, 0.111]$, $[-0.965, 0.185, 0.186]$, and $[0.160, -0.146, 0.976]$. The rotated axis vectors remain mutually orthogonal unit vectors with $\det(\mathbf{R}_{\mathrm{C}})=1$, but it is apparent that the first axis has experienced a substantial rotation to the North, the second a substantial rotation to the West, and the third has changed only slightly. An efficient way of representing these changes is with Euler angles which we compute using the MATLAB function `rotm2eul` with the default order of operations. For this, the series of rotations that transform $\mathbf{R}_{\mathrm{A}}$ to $\mathbf{R}_{\mathrm{C}}$ is as follows: anticlockwise rotation through an angle Φ_α about the initial $+z$ axis; anticlockwise rotation through and angle Φ_β about the new $+y'$ axis; anticlockwise rotation through an angle Φ_γ about the final $+x''$ axis. (Note that alternative ordering conventions are common.) For $\mathbf{R}_{\mathrm{C}}$ these angles are Φ_α=78.0°, Φ_β=−6.4°, and Φ_γ=10.8°.

5. Discussion

Modeling of medial moraine patterns, which was based on accepted understanding of the relevant processes and established simulation methods, was aimed at isolating glaciological influences on moraine patterns. As is well recognized, oscillating flow produces looped moraine patterns and these patterns are further complicated by variations in bed topography and spatial variations in bed friction. We find that spatial variations in surface mass balance have an insignificant influence on moraine patterns because such balance irregularities have little impact on flow dynamics (Figures 5c1 to 5c5).

The modeling study of S_0 stratification reinforces the point that patterns of S_0 can be unrelated to flow dynamics. Glacier flow can unquestionably influence the S_0 stratification, as evidenced in Figures 6c and 6e, but spatial variations in surface mass balance can greatly complicate the character of this stratification (Figure 6c). Temporal variations in balance bumps, not considered in this study, would contribute additional complexity. The implication for glaciologists is that attempts to associate S_0 patterns with ice flow irregularities demand caution.

The S_1 foliation has been observed in many locations and our efforts to explain them by modeling strain ellipsoids is persuasive. Working with a less sophisticated model, *Hooke & Hudleston* [1978] used similar thinking to reach similar conclusions. Much of the antecedent literature on the S_1 foliation emphasizes "shear" as a significant contributor to this foliation but the assertion is either simplistic or incomplete because shear is associated with all forms of ice deformation. Both simple shear and pure shear produce flattened strain ellipsoids, in our view an essential requirement for the S_1 foliation.

An important question for future effort is to identify the processes that link ice strain with foliation development. A significant role for air bubbles received early attention (*Hooke & Hudleston*, 1978) and is consistent with field observations on Trapridge Glacier (*Hambrey & Clarke*, 2019). This line of thinking raises question concerning the extent to which bubble geometry reflects the geometry of strain ellipsoids (e.g., *Alley & Fitzpatrick*, 1999; *Nakawo & Wakahama*, 1981). If the two are similar then one might imagine that strain ellipsoids that are flattened by horizontal compression, would produce bubbles that, when exposed by surface melting, would favor vertical penetration of meltwater and hence enhanced ice ablation. However, none of this has received scientific attention and, for now, the questions of if and how ice deformation could produce this foliation are unsettled.

As already noted, folding and thrusting are sub-grid processes that cannot be resolved using conventional ice dynamics models. Nested models, in which a high-resolution model having appropriate physics is embedded within a conventional ice dynamics model is an obvious step forward. Despite this disclaimer, we think our approach to characterizing folding using scalar invariants of a rank 3 tensor has wider potential. The gradient of the deformation gradient tensor $T_{ijk} = \partial_i F_{jk}$ has 12 scalar invariants and these might provide an efficient basis for categorizing the types of strain to which a glacier is subjected.

In *Hambrey & Clarke* [2019] there was poor quantitative agreement between measured and modeled crevasse trace orientations. The follow-up analysis in the present paper sheds additional light on the complexity of this undertaking and raises the question of whether this is a rewarding path to follow. Small differences in the model physics and strain history of ice parcels, for example the ice fracture model and the parcel location during surge episodes, can produce large differences in the simulation results and, we suggest,

in the observations as well. At this point, the best use of crevasse trace modeling is as a diagnostic tool to learn more about the sources of complexity. The use of diagnostic crevasse trace modeling to gain better understanding of S_2 foliation provides an example.

6. Concluding Remarks

In structural glaciology, as for many branches of the earth sciences, it can be challenging to confirm the links between processes and products. For glaciers, most of the relevant processes are slow and glaciers are sufficiently individual that comparing results from different glaciers has limited potential. Using numerical ice dynamics models to represent glaciers allows true experiments to be performed and hypotheses that are rooted in field observations to be formally tested. The power of such an approach depends on the skill of the computational model. Ice dynamics models have their own shortcomings and tend to be tailored to have skill at simulating the areal extent, thickness, and response time of a glacier. Advanced models also simulate layering and ice fabric. We suggest that models can be tested and improved by adding targets, such as ice structure, to the list.

In our work, the deformation gradient tensor $\mathbf{F}$ has played a central role because it encapsulates the total strain experienced by an ice parcel. Although the deformation gradient tensor is not new to the glaciological literature [e.g., *Hutter*, 1983; *Herzfeld et al.*, 2004; *Greve & Blatter*, 2009] its potential has not been exploited. We consider this to be a promising direction for model improvement. Evaluation of $\mathbf{F}$ currently involves ice trajectory calculations and integrations along these trajectories using the *McKenzie* [1979] algorithm. With Eulerian ice dynamics models this cumbersome approach may be unavoidable but finding something simpler would be a significant contribution.

Notation

$\mathcal{A}$	Temperature-dependent flow law coefficient [$\mathrm{M}^{-n}\,\mathrm{L}^{n}\,\mathrm{T}^{2n-1}$].
B	Bed surface elevation [L].
$\dot{b}$	Surface mass balance rate [$\mathrm{L}\,\mathrm{T}^{-1}$].
$[\mathrm{d}\dot{b}/\mathrm{d}z]_{\mathrm{abl}}$	Elevation gradient of mass balance in glacier ablation zone [T^{-1}].
$[\mathrm{d}\dot{b}/\mathrm{d}z]_{\mathrm{acc}}$	Elevation gradient of mass balance in glacier accumulation zone [T^{-1}].
$\mathcal{C}$	Sliding rate coefficient [$\mathrm{M}^{-m}\,\mathrm{L}^{m+1}\,\mathrm{T}^{2m-1}$].
$\mathcal{C}_{\mathrm{slide}}$	Sliding rate coefficient when not surging [$\mathrm{M}^{-m}\,\mathrm{L}^{m+1}\,\mathrm{T}^{2m-1}$].
$\mathcal{C}_{\mathrm{surge}}$	Sliding rate coefficient when surging [$\mathrm{M}^{-m}\,\mathrm{L}^{m+1}\,\mathrm{T}^{2m-1}$].
c	Specific heat capacity of ice [$\mathrm{L}^{2}\,\mathrm{T}^{-2}\,\Theta^{-1}$].
$\mathbf{D}$	Strain rate tensor [T^{-1}].
D_{jk}	Strain rate tensor in subscript notation [T^{-1}].
$\mathbf{F}$	Deformation gradient tensor [$\cdot$].
F_{jk}	Deformation gradient tensor in subscript notation [$\cdot$].
g	Gravity acceleration [$\mathrm{L}\,\mathrm{T}^{-2}$].
H	Ice thickness [L].
$\mathbf{I}$	Identity tensor [$\cdot$].
k	Thermal conductivity [$\mathrm{M}\,\mathrm{L}\,\mathrm{T}^{-3}\,\Theta^{-1}$].
$\mathbf{L}$	Velocity gradient tensor [T^{-1}].
L_{jk}	Velocity gradient tensor in subscript notation [T^{-1}].
L^{*}	Function controlling timing of surge cycle [$\cdot$].
M^{*}	Temporally- and spatially-varying sliding mask [$\cdot$].
m	Sliding law exponent [$\cdot$].
$\mathbf{N}_{k}^{\mathrm{U}}$	k-th eigenvector of $\mathbf{U}$ [$\cdot$].
$\mathbf{N}_{k}^{\mathrm{V}}$	k-th eigenvector of $\mathbf{V}$ [$\cdot$].
N_{jk}^{σ}	k-th eigenvector of σ_{jk} [$\cdot$].
n	Flow law exponent [$\cdot$].
$\mathbf{Q}$	Ice volume discharge per unit width [$\mathrm{L}^{2}\,\mathrm{T}^{-1}$].
$\mathcal{Q}_{2}$	Second quadratic invariant of T_{ijk} [L^{-2}].
$\mathbf{R}$	Rotation tensor [$\cdot$].
R_{jk}	Rotation tensor in subscript notation [$\cdot$].
S	Ice surface elevation [L].
s_{jk}	Deviatoric stress tensor [$\mathrm{M}\,\mathrm{L}^{-1}\,\mathrm{T}^{-2}$].

s_k k-th eigenvalue of s_{jk} [$\mathrm{M\,L^{-1}\,T^{-2}}$].
$\mathbf{T}$ Gradient of the deformation gradient tensor, $\mathbf{T} = \mathrm{grad}(\mathbf{F})$ [$\mathrm{L^{-1}}$].
T_{ijk} Gradient of the deformation gradient tensor in subscript notation, $T_{ijk} = \partial F_{jk}/\partial x_i$ [$\mathrm{L^{-1}}$].
T Ice temperature [Θ].
t Time [T].
t_d Depositional year [T].
$\mathbf{U}$ Right stretch tensor [$\cdot$].
U_{jk} Right stretch tensor in subscript notation [$\cdot$].
u x component of velocity vector [$\mathrm{L\,T^{-1}}$].
$\mathbf{V}$ Left stretch tensor [$\cdot$].
V_{jk} Left stretch tensor in subscript notation [$\cdot$].
$\mathbf{v}$ Ice velocity [$\mathrm{L\,T^{-1}}$].
v_k Ice velocity in subscript notation [$\mathrm{L\,T^{-1}}$].
$\mathbf{v}_\mathrm{s}$ Glacier sliding velocity [$\mathrm{L\,T^{-1}}$].
v y component of velocity vector [$\mathrm{L\,T^{-1}}$].
$\mathbf{W}$ Spin tensor [$\mathrm{T^{-1}}$].
W_{jk} Spin tensor in subscript notation [$\mathrm{T^{-1}}$].
w z component of velocity vector [$\mathrm{L\,T^{-1}}$].
$\mathbf{X}$ Spatial coordinates of an ice particle [L].
X_k Spatial coordinates of an ice particle in subscript notation [L].
x Easting distance coordinate [L].
y Northing distance coordinate [L].
Z_ela Equilibrium line altitude [L].
z Vertical distance coordinate [L].
Δt Time increment [T].
δ_{jk} Kronecker delta (identify tensor in subscript notation) [$\cdot$].
ζ Vertically-stretched coordinate, $\zeta = (z - B)/H$ [$\cdot$].
η Ice viscosity [$\mathrm{M\,L^{-1}\,T^{-1}}$].
$\kappa_{1:2}$ Eigenvalue ratio, $\kappa_{1:2} = \lambda_1^\mathrm{U}/\lambda_2^\mathrm{U}$ [$\cdot$].
$\kappa_{2:3}$ Eigenvalue ratio, $\kappa_{2:3} = \lambda_2^\mathrm{U}/\lambda_3^\mathrm{U}$ [$\cdot$].

$\lambda_k^{\mathbf{U}}$ k-th eigenvalue of $\mathbf{U}$ $[\cdot]$.
$\lambda_k^{\mathbf{V}}$ k-th eigenvalue of $\mathbf{V}$ $[\cdot]$.
ξ Vertically-stretched coordinate, $\xi = (z - B)/H$ $[\cdot]$.
ρ Density of ice $[\mathrm{M\,L^{-3}}]$.
σ_{jk} Stress tensor $[\mathrm{M\,L^{-1}\,T^{-2}}]$.
σ_k k-th eigenvalue of σ_{jk} $[\mathrm{M\,L^{-1}\,T^{-2}}]$.
τ Effective stress $[\mathrm{M\,L^{-1}\,T^{-2}}]$.
Ψ A generalized passive tracer [problem-dependent].
∇_{xy} Two-dimensional gradient operator $[\mathrm{L^{-1}}]$.

Acknowledgments. The field work and model development were supported by grants to GKCC from the Natural Sciences and Engineering Research Council of Canada. MJH acknowledges the award of a Visiting Professorship at the University of British Columbia. Valuable discussions with Christian Schoof and Elisa Mantelli were greatly appreciated. The suggestions and constructive criticisms of reviewer Ed Waddington, an anonymous reviewer, and Editor-in-Chief Bryn Hubbard are greatly appreciated. There are no observational data in this study. Scripts and data files used to produce the modeling results and associated figures were placed in a GitHub repository and can be accessed at https://doi.org/10.5281/zenodo.1491931.

References

Agassiz, L. (1840). *Études sur les glaciers*. 346 pp., Jent et Gassman, Neuchâtel, Switzerland.

Ahmad, F. (2011). Invariants of a Cartesian tensor of rank 3. *Archives of Mechanics*, *63*(4), 383–392.

Allen, C. R., Kamb, W. B., Meier, M. F., & Sharp, R. P. (1960). Structure of the lower Blue Glacier, Washington. *Journal of Geology*, *68*, 601–625. https://doi.org/10.1086/626700

Alley, R. B., & Fitzpatrick, J. J. (1999). Conditions for bubble elongation in cold ice-sheet ice. *Journal of Glaciology*, *45*(149), 147–153. https://doi.org/10.1017/S0022143000003129

Brannon, R. M. (2018). *Rotation, Reflection, and Frame Changes. Orthogonal Tensors in Computational Engineering Mechanics*. Bristol: IOP Publishing.

https://doi.org/10.1088/978-0-7503-1454-1

Clarke, G. K. C., & Blake, E. W. (1991). Geometric and thermal evolution of a surge-type glacier in its quiescent state: Trapridge Glacier, Yukon Territory, Canada, 1969–89. *Journal of Glaciology*, *37*(125), 158–169. https://doi.org/10.3189/s002214300004291x

Clarke, G. K. C., & Marshall, S. J. (2002). Isotopic balance of the Greenland Ice Sheet: modelled concentrations of water isotopes from 30,000 BP to present. *Quaternary Science Reviews*, *21*, 419–430. https://doi.org/10.1016/S0277-3791(01)00111-1

Clarke, G. K. C., Lhomme, N., & S. J. Marshall (2005). Tracer transport in the Greenland ice sheet: three-dimensional isotopic stratigraphy. *Quaternary Science Reviews*, *24*, 155–171. https://doi.org/10.1016/j.quascirev.2004.08.021

Clarke, G. K. C., Anslow, F. S., Jarosch, A. H., Radić, V., Menounos, B., Bolch, T., & Berthier, E. (2013). Ice volume and subglacial topography for western Canadian glaciers from mass balance fields, thinning rates, and a bed stress model. *Journal of Climate*, *26*, 4282–4303. https://doi.org/10.1175/JCLI-D-12-00513.1

Clarke, G. K. C., Jarosch, A. H., Anslow, F. S., Radić, V., & Menounos, B. (2015). Projected deglaciation of western Canada in the twenty-first century. *Nature Geoscience*, *8*, 372–377. https://doi.org/10.1038/ngeo2407

Cuffey, K. M., & Paterson, W. S. B. (2010). *The Physics of Glaciers* (4th ed.). Burlington: Elsevier. https://doi.org/10.3189/002214311798843412

Flowers, G. E., & Clarke, G. K. C. (1999). Surface and bed topography of Trapridge Glacier, Yukon Territory, Canada: digital elevation models and derived hydraulic geometry. *Journal of Glaciology*, *45*(149), 165–174. https://doi.org/10.1017/S0022143000003142

Forbes, J. D. (1842). First letter on glaciers. Courmayeur, Piedmont, 4 July 1842. *Edinburgh New Philosophical Journal*, *33*(66), 338–41.

Frappé-Sénéclauze, T.-P., & Clarke, G. K. C. (2007). Slow surge of Trapridge Glacier, Yukon Territory, Canada. *Journal of Geophysical Research*, *112*, F03S32. https://doi.org/10.1029/2006JF0040607

Gay, N. C. (1968). Pure shear and simple shear deformation of inhomogeneous viscous fluids. 1. Theory. *Tectonophysics*, *5*(4), 295–302. https://doi.org/10.1016/0040-1951(68)90065-6

Glen, J. W. (1955). The creep of polycrystalline ice. *Proceedings of the Royal Society of London. Series A, Mathematical and Physical Sciences*, *228*(1175), 519–538. https://doi.10.1098/rspa.1955.0066

Goelles, T., Grosfeld, K., & Lohmann, G. (2014). Semi-Lagrangian transport of oxygen isotopes in polythermal ice sheets: implementation and first results. *Geoscientific Model Development*, *7*, 1395–1408. https://doi.org/10.5194/gmd-7-1395-2014

Greve, R., & Blatter, H. (2009). *Dynamics of Ice Sheets and Glaciers*. Berlin: Springer-Verlag

Hambrey, M. J., & Clarke, G. K. C. (2019). Structural evolution during cyclic glacier surges: 1. Structural glaciology of Trapridge Glacier, Yukon, Canada. *Journal of Geophysical Research*, DOI: 10.1029/2018JF004869.

Hambrey, M. J., & Milnes, A. G. (1978). Structural geology of an Alpine glacier. *Eclogae Geologicae Helvetiae*, *70*, 667–684.

Hambrey, M. J., & Müller, F. (1978). Ice deformation and structures in the White Glacier, Axel Heiberg Island, Northwest Territories, Canada. *Journal of Glaciology*, *20*(82), 41–

66. https://doi.org/10.3189/S0022143000021213

Hambrey, M. J., Murray, T., Glasser, N. F., Hubbard, A., Hubbard, B., Stuart, G., ... Kohler, J. (2005). Structure and changing dynamics of a polythermal valley glacier on a centennial timescale: Midre Lovénbreen, Svalbard. *Journal of Geophysical Research*, *110*(F1), F01006. https://doi.org/10.1029/2004JF000128

Herzfeld, U. C., Clarke, G. K. C., Mayer, H., & Greve, R. (2004). Derivation of deformation characteristics in fast-moving glaciers. *Computers & Geosciences*, *30*, 291–302. https://doi.org/10.1016/j.cageo.2003.10.012

Hooke, R. LeB., & Hudleston, P. J. (1978). Origin of foliation in glaciers. *Journal of Glaciology*, *20*(83), 285–299. https://doi.org/10.3189/S0022143000013848

Hubbard, B., & Glasser, N. (2005). *Field Techniques in Glaciology and Glacial Geomorphology*. Chichester: John Wiley.

Hubbard, A., & Hubbard, B. (2000). The potential contribution of high-resolution glacier flow modelling to structural glaciology. *Geological Society, London, Special Publications*, *176*, 135–146. https://doi.org/10.1144/GSL.SP.2000.176.01.10

Hudleston, P. J. (1977). Progressive deformation and development of fabric across zones of shear in glacial ice. In S. Saxena, S. Bhattacharji (Eds.), *Energetics of geological processes* (pp. 121–150). Amsterdam: Springer-Verlag. https://doi.org/10.1007/978-3-642-86574-9_7

Hutter, K. (1983). *Theoretical Glaciology*. Dordrecht: D. Reidel.

Hutter, K., & Jöhnk, K. D. (2004). *Continuum Methods of Physical Modeling*. Berlin: Springer-Verlag.

Jarosch, A. H., Schoof, C. G., & Anslow, F. S. (2013). Restoring mass conservation to shallow ice flow models over complex terrain. *The Cryosphere*, *7*, 229–240. https://doi.org/10.5194/tc-7-229-2013

Lhomme, N., Clarke, G. K. C., & Marshall, S. J. (2005). Tracer transport in the Greenland Ice Sheet: constraints on ice cores and glacial history. *Quaternary Science Reviews*, *24*, 173–194. https://doi.org/10.1016/j.quascirev.2004.08.020

Malvern, L. E. (1969). *Introduction to the Mechanics of a Continuous Medium*. Englewood Cliffs: Prentice-Hall.

McKenzie, D. (1979). Finite deformation during fluid flow. *Geophysical Journal of the Royal Astronomical Society*, *58*, 689–715. https://doi.org/10.1111/j.1365-246X.1979.tb04803.x

Marshall, S. J., Tarasov, L., Clarke, G. K. C., & Peltier, W. R. (2000). Glaciological reconstruction of the Laurentide Ice Sheet: physical processes and modelling challenges. *Canadian Journal of Earth Sciences*, *37*, 769–793. https://doi.org/10.1139/e99-113

Nakawo, M., & Wakahama, G. (1981). Preliminary experiments on the formation of elongated air bubbles in glacier ice by stress. *Journal of Glaciology*, *27*(95), 141–146. https://doi.org/10.3189/S0022143000011291

Nye, J. F. (1957). The distribution of stress and velocity in glaciers and ice sheets. *Proceedings of the Royal Society A: Mathematical, Physical and Engineering Sciences*, *23*(1216), 113–133. https://doi.org/10.1098/rspa.1957.0026

Ramsay, J. G. (1967). *Folding and Fracturing of Rocks*. New York: McGraw-Hill.

Seddik, H., Greve, R., Zwinger, T., & Placidi, L. (2011). A full Stokes ice flow model for the vicinity of Dome Fuji, Antarctica, with induced anisotropy and fabric evolution.

The Cryosphere, *5*, 495–508. https://doi.org/10.5194/tc-5-495-2011

Staniforth, A., & Côté, J. (1991). Semi-Lagrangian integration schemes for atmospheric models—A review. *Monthly Weather Review*, *119*, 2206–2223. https://doi.org/10.1175/1520-0493(1991)119¡2206:SLISFA¿2.0.CO;2

Strang, G. (2007). *Computational Science and Engineering*. Wellesley: Wellesley-Cambridge Press.

van der Veen, C. J. (1999). *Fundamentals of Glacier Dynamics*. Rotterdam: Balkema Publishers.

van der Veen, C. J. (2007). Fracture propagation as means of rapidly transferring surface meltwater to the base of glaciers. *Geophysical Research Letters*, *34*, L01501. https://doi.org/10.1029/2006GL028385

Waddington, E. D., & Clarke, G. K. C. (1988). Stable-isotope pattern predicted in surge-type glaciers. *Canadian Journal of Earth Sciences*, *25*(5), 657–668. https://doi.org/10.1139/e88-063

Table 1. Physical properties and parameters of the Traplike reference model

Property	Value	Units
Ice density, ρ	900	$\mathrm{kg\,m^{-3}}$
Water density, ρ_w	1000	$\mathrm{kg\,m^{-3}}$
Gravity acceleration, g	9.80	$\mathrm{m\,s^{-2}}$
Creep coefficient, $\mathcal{A}_0$	7.42×10^5	$\mathrm{Pa^{-3}\,yr^{-1}}$
Creep exponent, n	3	
Creep activation energy, E	115	$\mathrm{kJ\,mol^{-1}}$
Gas constant, R	8.314462	$\mathrm{J\,mol^{-1}\,K^{-1}}$
Kelvin temperature, T_K	273.15	C
Residual ice viscosity, η_0	1.0×10^{15}	Pa s
Equilibrium line altitude, Z_ela	2475	m
Mass balance gradient (accumulation), $[\mathrm{d}\dot{b}/\mathrm{d}z]_\mathrm{acc}$	3.8095×10^{-3}	$\mathrm{yr^{-1}}$
Mass balance gradient (ablation), $[\mathrm{d}\dot{b}/\mathrm{d}z]_\mathrm{abl}$	7.6190×10^{-3}	$\mathrm{yr^{-1}}$
Sliding coefficient (non-surging), $\mathcal{C}_\mathrm{slide}$	5.0×10^{-11}	$\mathrm{m\,yr^{-1}\,Pa^{-2}}$
Sliding coefficient (surging), $\mathcal{C}_\mathrm{surge}$	2.5×10^{-9}	$\mathrm{m\,yr^{-1}\,Pa^{-2}}$
Sliding exponent, m	2	
Surge cycle, Δt_cycle	13	yr
Surge peak time, Δt_peak	11	yr
Width of surge front, ΔL	150	m
Thermal conductivity parameter, k_0	9.828	$\mathrm{W\,m^{-1}\,K^{-1}}$
Thermal conductivity parameter, k_1	0.0057	$\mathrm{K^{-1}}$
Specific heat capacity parameter, c_0	152.5	$\mathrm{J\,kg^{-1}\,K^{-1}}$
Specific heat capacity parameter, c_1	7.122	$\mathrm{J\,kg^{-1}\,K^{-2}}$
Pressure melting temperature coefficient, β	8.7×10^{-4}	$\mathrm{K\,m^{-1}}$
Grid spacing, Δx and Δy	30	m
Outer time step, Δt	0.01	yr
Easting dimension of computational grid, N_x	144	
Northing dimension of computational grid, N_y	57	
Vertical levels for ξ grid, N_ξ	21	
Vertical levels for ζ grid, N_ζ	11	

Table 2. Tensor values along a particle trajectory

Tensor	Start year 1886.99	Intermediate year 1980.00	End year 2006.60
$\mathbf{F}$	$\begin{bmatrix} 1 & 0 & 0 \\ 0 & 1 & 0 \\ 0 & 0 & 1 \end{bmatrix}$	$\begin{bmatrix} 1.209 & -4.199 & 0.239 \\ 0.379 & -0.552 & 0.046 \\ -0.078 & 1.074 & 1.037 \end{bmatrix}$	$\begin{bmatrix} 0.718 & -3.183 & 0.208 \\ 0.305 & -0.014 & 0.024 \\ 0.113 & 0.514 & 1.024 \end{bmatrix}$
$\mathbf{U}$	$\begin{bmatrix} 1 & 0 & 0 \\ 0 & 1 & 0 \\ 0 & 0 & 1 \end{bmatrix}$	$\begin{bmatrix} 0.561 & -1.125 & 0.178 \\ -1.125 & 4.221 & 0.054 \\ 0.178 & 0.054 & 1.049 \end{bmatrix}$	$\begin{bmatrix} 0.458 & -0.616 & 0.180 \\ -0.616 & 3.165 & -0.006 \\ 0.180 & -0.006 & 1.030 \end{bmatrix}$
$\lambda^{\mathbf{U}}_{jk}$	$\begin{bmatrix} 1 & 0 & 0 \\ 0 & 1 & 0 \\ 0 & 0 & 1 \end{bmatrix}$	$\begin{bmatrix} 4.539 & 0 & 0 \\ 0 & 1.089 & 0 \\ 0 & 0 & 0.202 \end{bmatrix}$	$\begin{bmatrix} 3.299 & 0 & 0 \\ 0 & 1.070 & 0 \\ 0 & 0 & 0.283 \end{bmatrix}$
$\mathbf{N^U}$	$\begin{bmatrix} 1 & 0 & 0 \\ 0 & 1 & 0 \\ 0 & 0 & 1 \end{bmatrix}$	$\begin{bmatrix} 0.272 & 0.207 & -0.940 \\ -0.962 & 0.057 & -0.266 \\ -0.001 & 0.977 & 0.215 \end{bmatrix}$	$\begin{bmatrix} 0.213 & 0.219 & -0.952 \\ -0.977 & 0.067 & -0.203 \\ 0.020 & 0.973 & 0.228 \end{bmatrix}$
$\mathbf{V}$	$\begin{bmatrix} 1 & 0 & 0 \\ 0 & 1 & 0 \\ 0 & 0 & 1 \end{bmatrix}$	$\begin{bmatrix} 4.264 & 0.600 & -0.779 \\ 0.600 & 0.293 & -0.068 \\ -0.779 & -0.068 & 1.274 \end{bmatrix}$	$\begin{bmatrix} 3.254 & 0.080 & -0.308 \\ 0.080 & 0.290 & 0.055 \\ -0.308 & 0.055 & 1.108 \end{bmatrix}$
$\lambda^{\mathbf{V}}_{jk}$	$\begin{bmatrix} 1 & 0 & 0 \\ 0 & 1 & 0 \\ 0 & 0 & 1 \end{bmatrix}$	$\begin{bmatrix} 4.539 & 0 & 0 \\ 0 & 1.089 & 0 \\ 0 & 0 & 0.202 \end{bmatrix}$	$\begin{bmatrix} 3.299 & 0 & 0 \\ 0 & 1.070 & 0 \\ 0 & 0 & 0.283 \end{bmatrix}$
$\mathbf{N^V}$	$\begin{bmatrix} 1 & 0 & 0 \\ 0 & 1 & 0 \\ 0 & 0 & 1 \end{bmatrix}$	$\begin{bmatrix} 0.962 & 0.222 & -0.155 \\ 0.140 & 0.085 & 0.987 \\ -0.233 & 0.971 & -0.050 \end{bmatrix}$	$\begin{bmatrix} 0.990 & 0.136 & -0.035 \\ 0.024 & 0.083 & 0.996 \\ -0.139 & 0.987 & -0.079 \end{bmatrix}$
$\mathbf{R}$	$\begin{bmatrix} 1 & 0 & 0 \\ 0 & 1 & 0 \\ 0 & 0 & 1 \end{bmatrix}$	$\begin{bmatrix} 0.162 & -0.955 & 0.250 \\ 0.983 & 0.133 & -0.129 \\ 0.090 & 0.266 & 0.960 \end{bmatrix}$	$\begin{bmatrix} 0.207 & -0.965 & 0.160 \\ 0.972 & 0.185 & -0.146 \\ 0.111 & 0.186 & 0.976 \end{bmatrix}$

Table 2. Continued. Tensor values along a particle trajectory

Tensor	Start year 1886.99	Intermediate year 1980.00	End year 2006.60
σ_{jk}	$\begin{bmatrix} 17.75 & -67.74 & 0.15 \\ -67.74 & 38.14 & 13.82 \\ 0.15 & 13.82 & -0.04 \end{bmatrix}$	$\begin{bmatrix} -296.50 & -54.05 & 15.71 \\ -54.05 & -223.20 & 12.83 \\ 15.71 & 12.83 & -184.91 \end{bmatrix}$	$\begin{bmatrix} -52.82 & -36.51 & 7.61 \\ -36.51 & -6.15 & 6.88 \\ 7.61 & 6.88 & -0.00 \end{bmatrix}$
λ^{σ}_{jk}	$\begin{bmatrix} 97.56 & 0 & 0 \\ 0 & 0.84 & 0 \\ 0 & 0 & -42.55 \end{bmatrix}$	$\begin{bmatrix} -181.00 & 0 & 0 \\ 0 & -195.69 & 0 \\ 0 & 0 & -327.93 \end{bmatrix}$	$\begin{bmatrix} 14.28 & 0 & 0 \\ 0 & 0.91 & 0 \\ 0 & 0 & -74.16 \end{bmatrix}$
$\mathbf{N}^{\sigma}$	$\begin{bmatrix} -0.643 & 0.231 & 0.730 \\ 0.758 & 0.060 & 0.649 \\ 0.106 & 0.971 & -0.214 \end{bmatrix}$	$\begin{bmatrix} -0.015 & 0.487 & 0.873 \\ 0.308 & -0.829 & 0.468 \\ 0.951 & 0.276 & -0.138 \end{bmatrix}$	$\begin{bmatrix} 0.455 & 0.202 & 0.867 \\ -0.873 & -0.094 & 0.479 \\ -0.179 & 0.975 & -0.133 \end{bmatrix}$

Data in the 1886.99 column correspond to point A in Figure 3, 1980.00 to point B, and 2006.60 to Point C. Units of σ_{jk} and λ^{σ}_{jk} are kPa.

Table 3. Strain ellipsoids for centerline sites and selected off-line sites of the Traplike Glacier reference model at 2006.6

Site	Deposition date	k	$\lambda_k^{\mathbf{V}}$	$\mathbf{N}_k^{\mathbf{V}}$			Axis ratios		Dip	Status
				$N_x^{\mathbf{V}}$	$N_y^{\mathbf{V}}$	$N_z^{\mathbf{V}}$	$\kappa_{1:2}$	$\kappa_{2:3}$	δ_3	
E1.5C	1942.7	1	1.227	−1.000	0.000	−0.022	1.25	1.17	1.2°	Fail ($\kappa_{2:3}$,δ_3)
		2	0.978	0.000	1.000	0.000				
		3	0.833	0.022	0.000	−1.000				
E2C	1923.0	1	2.416	−0.999	0.000	0.054	2.70	1.93	90.0°	Fail ($\kappa_{2:3}$)
		2	0.894	0.054	0.000	0.999				
		3	0.463	−0.000	−1.000	0.000				
E2.5C	1910.9	1	2.792	−1.000	0.000	0.009	2.42	3.73	90.0°	Fail ($\kappa_{2:3}$)
		2	1.155	0.009	0.000	1.000				
		3	0.310	−0.000	−1.000	0.000				
E3.5C	1876.7	1	3.042	−0.819	0.000	−0.575	2.92	3.30	90.0°	Fail ($\kappa_{2:3}$)
		2	1.041	0.575	−0.000	−0.819				
		3	0.316	0.000	1.000	−0.000				
E3C	1893.8	1	3.122	−0.996	0.000	−0.093	2.44	5.09	90.0°	Pass
		2	1.277	0.093	−0.000	−0.996				
		3	0.251	0.000	1.000	−0.000				
E3S1	1904.3	1	3.038	0.979	−0.061	0.196	2.01	6.93	89.6°	Pass
		2	1.511	−0.196	0.005	0.980				
		3	0.218	0.060	0.998	0.007				
E3S2	1902.7	1	1.840	0.959	0.253	0.125	1.86	1.81	81.6°	Fail ($\kappa_{2:3}$)
		2	0.990	−0.082	−0.175	0.981				
		3	0.549	0.271	−0.951	−0.147				
E3S3	1887.0	1	3.300	0.990	−0.024	−0.139	3.08	3.78	85.5°	Fail ($\kappa_{2:3}$)
		2	1.070	−0.136	0.083	−0.987				
		3	0.283	−0.035	−0.996	−0.079				
E4C	1854.1	1	8.139	−0.978	0.000	−0.209	20.40	1.30	12.1°	Fail ($\kappa_{2:3}$)
		2	0.399	−0.000	−1.000	0.000				
		3	0.308	−0.209	0.000	0.978				

Table 3. Continued: Strain ellipsoids for centerline sites and selected off-line sites of the Traplike Glacier reference model at 2006.6

Site	Deposition date	k	$\lambda_k^{\mathbf{V}}$	$\mathbf{N}_k^{\mathbf{V}}$			Axis ratios		Dip	Status
				$N_x^{\mathbf{V}}$	$N_y^{\mathbf{V}}$	$N_z^{\mathbf{V}}$	$\kappa_{1:2}$	$\kappa_{2:3}$	δ_3	
E4.5C	1835.4	1	18.744	−0.997	−0.000	0.074	64.85	1.57	4.3°	Fail ($\kappa_{2:3}$,δ_3)
		2	0.289	−0.000	1.000	−0.000				
		3	0.185	−0.074	−0.000	−0.997				
E4.5S1	1809.0	1	17.679	0.984	0.103	−0.147	24.71	9.06	45.6°	Pass
		2	0.716	0.177	−0.692	0.699				
		3	0.079	0.030	0.714	0.699				
E4.5S2	1741.2	1	14.479	−0.982	−0.062	0.179	24.06	5.24	22.6°	Fail (δ_3)
		2	0.602	−0.121	0.932	−0.340				
		3	0.115	0.145	0.356	0.923				
E4.5S3	1693.3	1	23.081	0.488	−0.872	−0.041	34.06	10.60	4.4°	Fail (δ_3)
		2	0.678	−0.869	−0.490	0.065				
		3	0.064	0.077	−0.004	0.997				
E5C	1822.0	1	16.820	0.994	−0.000	−0.110	66.11	1.09	6.3°	Fail ($\kappa_{2:3}$)
		2	0.254	0.000	−1.000	0.001				
		3	0.234	−0.110	−0.001	−0.994				
E5S1	1787.5	1	19.239	0.974	−0.183	−0.136	23.10	13.35	56.8°	Pass
		2	0.833	0.010	−0.565	0.825				
		3	0.062	−0.228	−0.805	−0.548				
E5S2	1590.4	1	20.652	−0.939	−0.111	0.325	7.07	176.17	20.1°	Fail (δ_3)
		2	2.921	−0.155	0.981	−0.113				
		3	0.017	−0.306	−0.157	−0.939				

To save space we have excluded sites that lie to the north of the centerline. These are mirror images of the southern sites. Results for site E1C are omitted because of inaccuracy of the trajectory integrations.

Table 4. Total rotation of ice emerging at measurement sites near the terminus of Traplike Glacier reference model at 2006.6

Site	Deposition date	Euler angles Φ_α	Φ_β	Φ_γ
Centerline				
E3C	1893.8	0.0	2.4	0.0
E3.5C	1876.7	0.0	3.0	0.0
E4C	1854.1	0.0	24.9	0.0
E4.5C	1835.4	0.0	42.1	0.0
E5C	1822.0	0.0	47.8	0.0
South line				
E3S1	1904.3	−73.7	−6.35	−2.80
E3.5S1	1878.8	−60.7	0.4	−10.1
E4S1	1845.3	−7.37	27.4	−16.9
E4.5S1	1809.0	−11.8	42.8	−16.1
E5S1	1787.5	−28.8	48.1	−28.1

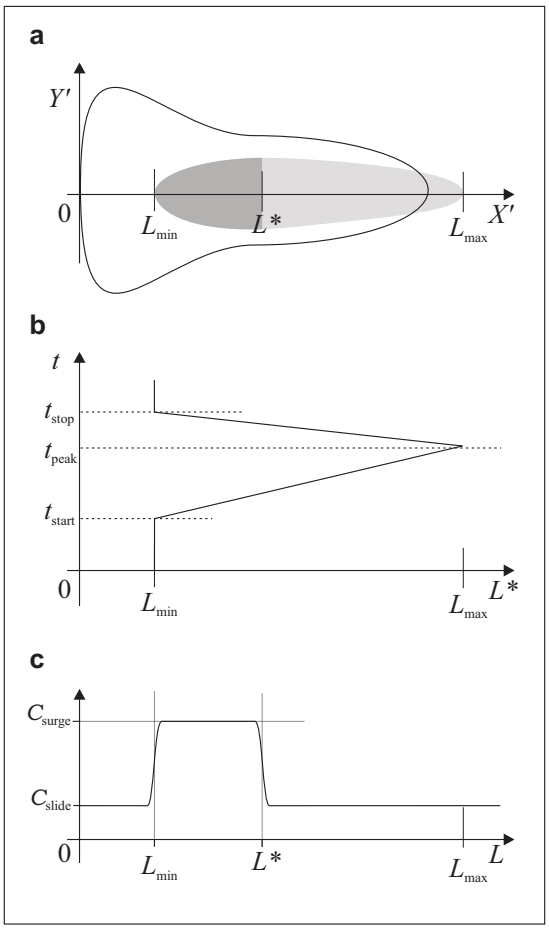

Figure 1. Zone of fast sliding. (a) Plan view showing glacier outline and outline of zone of enhanced sliding. Dark shading corresponds to fast sliding; light shading indicates the maximum extent of the fast-sliding zone. (b) Temporal evolution of $L^*(t)$. (c) Downflow variation of the sliding rate parameter $\mathcal{C}$.

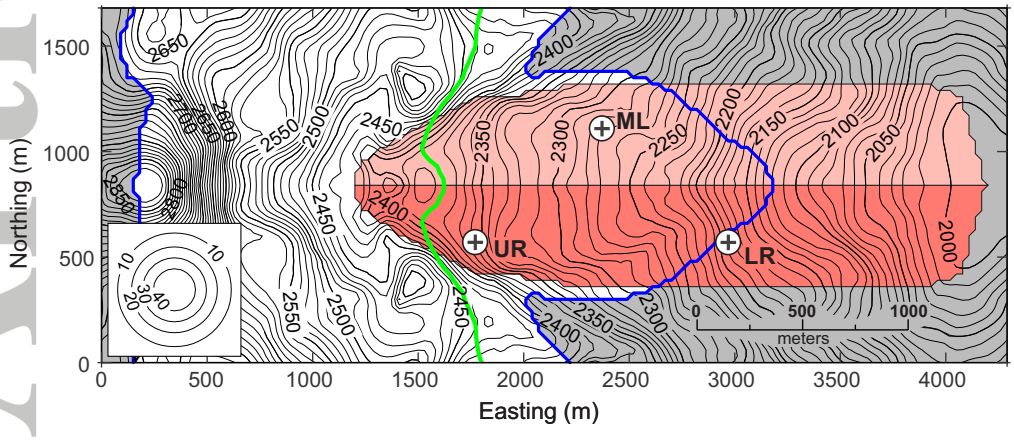

Figure 2. Bed topography for the Traplike Glacier reference model. The post-surge ice extent is indicated by a blue outline. Zones where bed sliding friction is subject to cyclic changes are indicated by shading (light pink for the north zone and dark pink for the south). The center points for optional bed bumps are indicated by bold "+" symbols. The upper right (UR), middle left (ML), and lower right (LR) bump positions are labeled. Elevation contours are in meters with a contour interval of 10 m. The arrow indicates the direction of grid North. Inset: Topography of a bed bump.

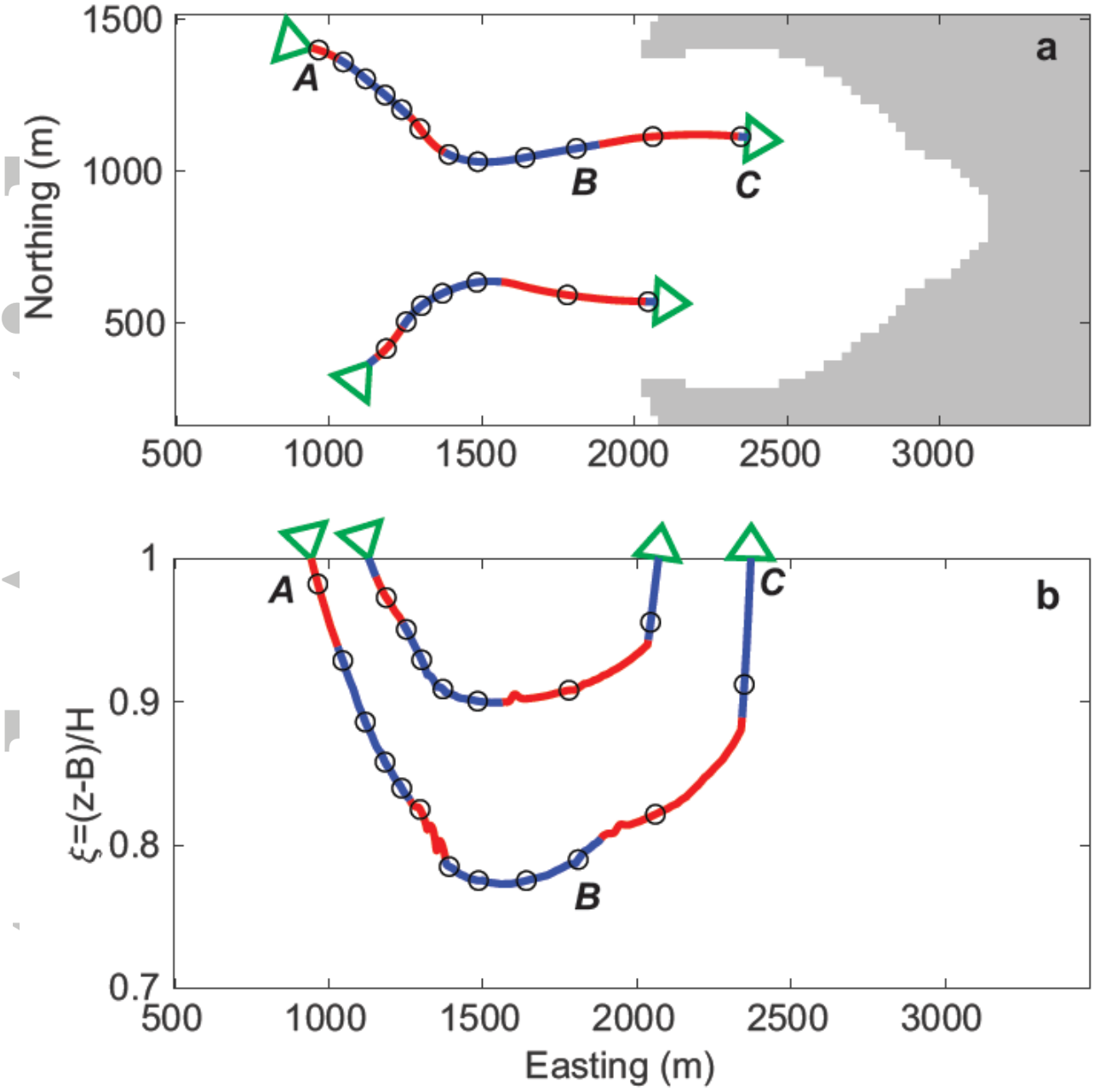

Figure 3. Simulated particle trajectories for two measurement sites and the Traplike Glacier reference model. (a) Map view. (b). Profile view with a stretched vertical coordinate $\xi=(z-B)/H$ where $\xi=1$ corresponds to the glacier surface and $\xi=0$ to the bed. For both plots, segments of the trajectory that are associated with surging are plotted in red, and non-surging segments in blue.

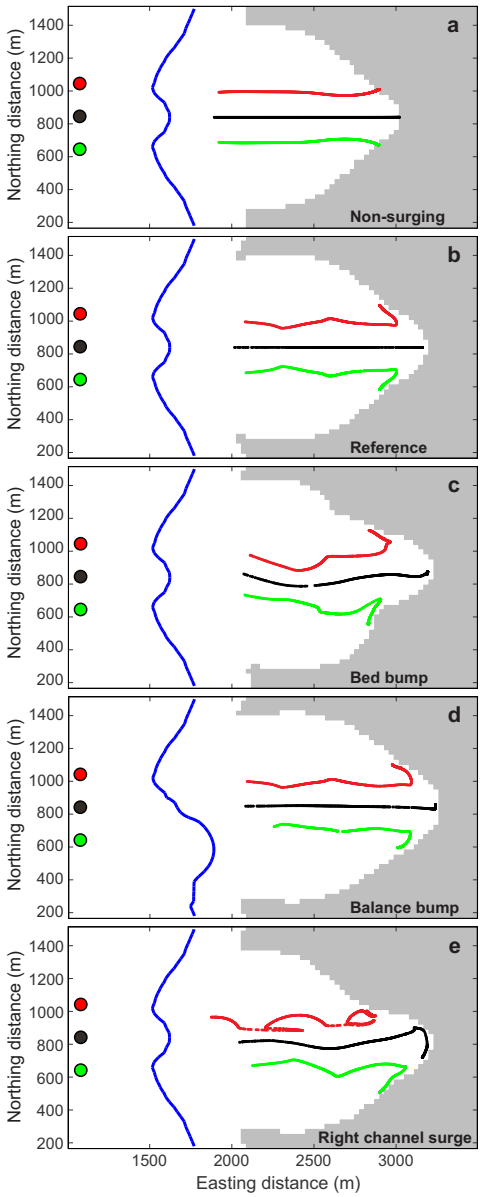

Figure 4. Maps of simulated medial moraine patterns immediately following surge termination (year 13 of the surge cycle or 1998 for Trapridge Glacier). The ELA is indicated (blue line) as well as source points for moraine debris and the associated supraglacial debris tracks. The colored circle markers near the left map boundary indicate points where moraine debris is added at the glacier surface. (a) Traplike non-surging model. (b) Traplike reference model. (c) Traplike bed bump model. (d) Traplike balance bump model. (e) Traplike right channel surge.

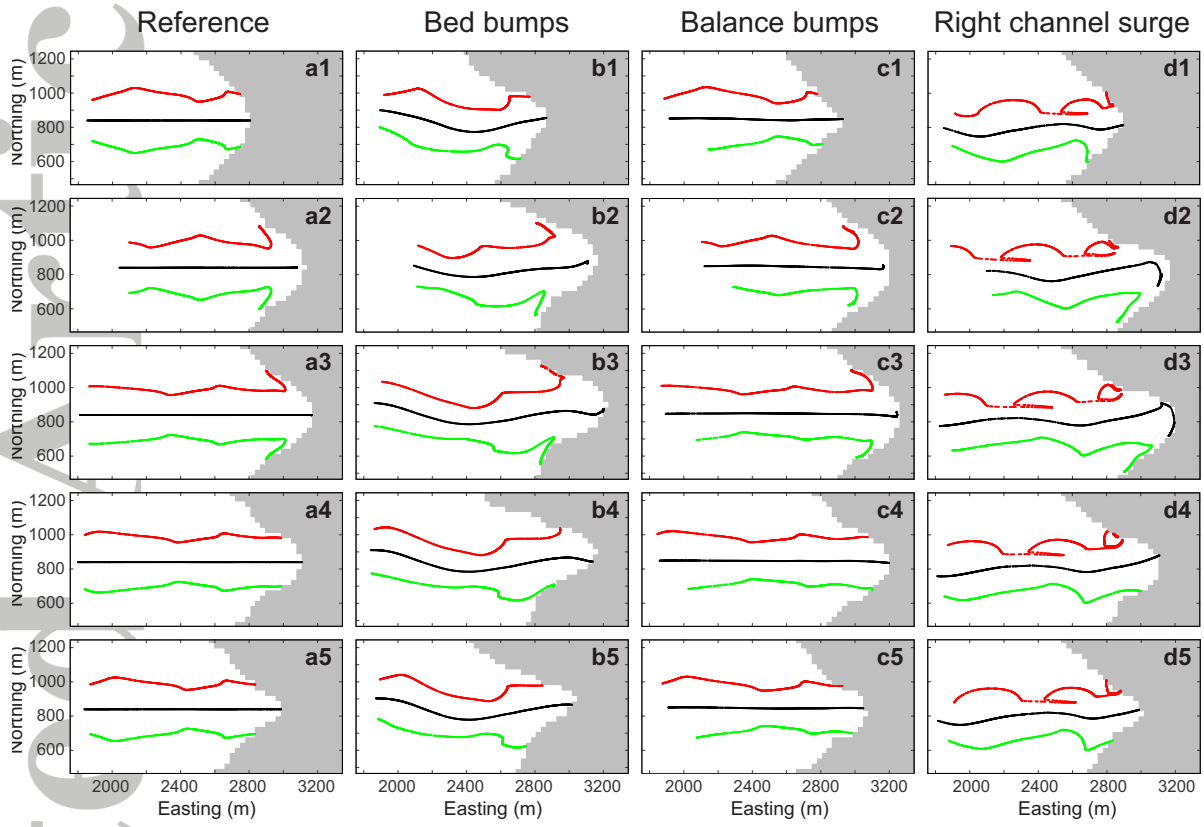

Figure 5. Maps of simulated medial moraine patterns. (a1–a5) Traplike reference model. (b1–b5) Traplike bed bump. (c1–c5) Traplike balance bump. (d1–d5) Traplike right channel surge. Output is for Years 0, 10, 20, 30, and 40 of the 50-year surge cycle. In terms of Trapridge Glacier calendar years these correspond to $1985 \pm N$, $1995 \pm N$, $2005 \pm N$. $1965 \pm N$ and $1975 \pm N$ where N is any integer.

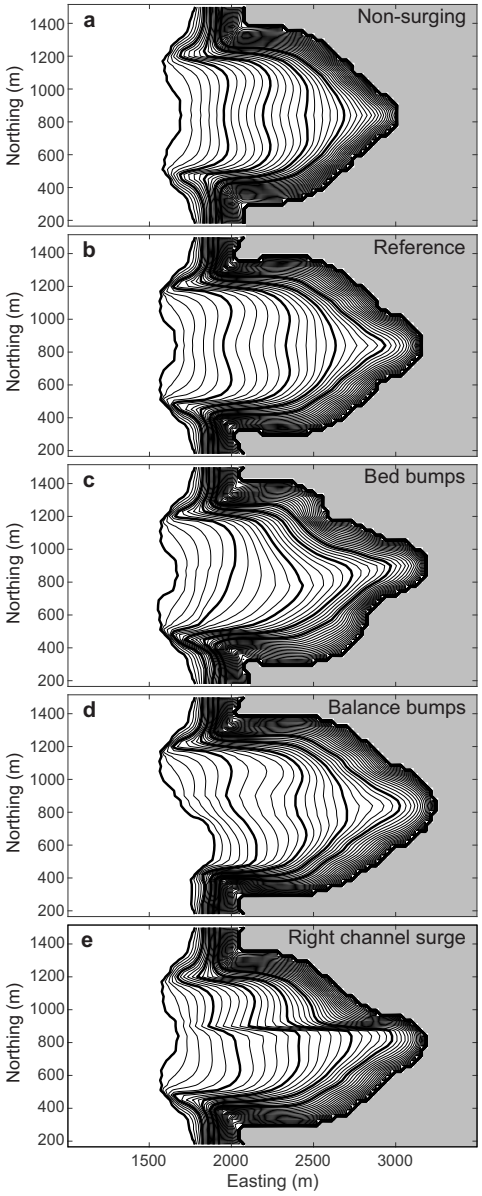

Figure 6. Maps of simulated primary stratification S_0 for observation year 2006.6 (year 21.6 of the modeled surge cycle). The contours delineate the exposed isochronal surfaces and therefore are not plotted for the accumulation zone. The contour interval is 10 years with bold contours every 50 years. The uppermost bold contour corresponds to year 2000 and approximates the ELA (which would be the 2006.6 contour). (a) Non-surging model. (b) Traplike reference model. (c) Traplike bed bump model. (d) Traplike balance bump model. (e) Traplike right channel surge model.

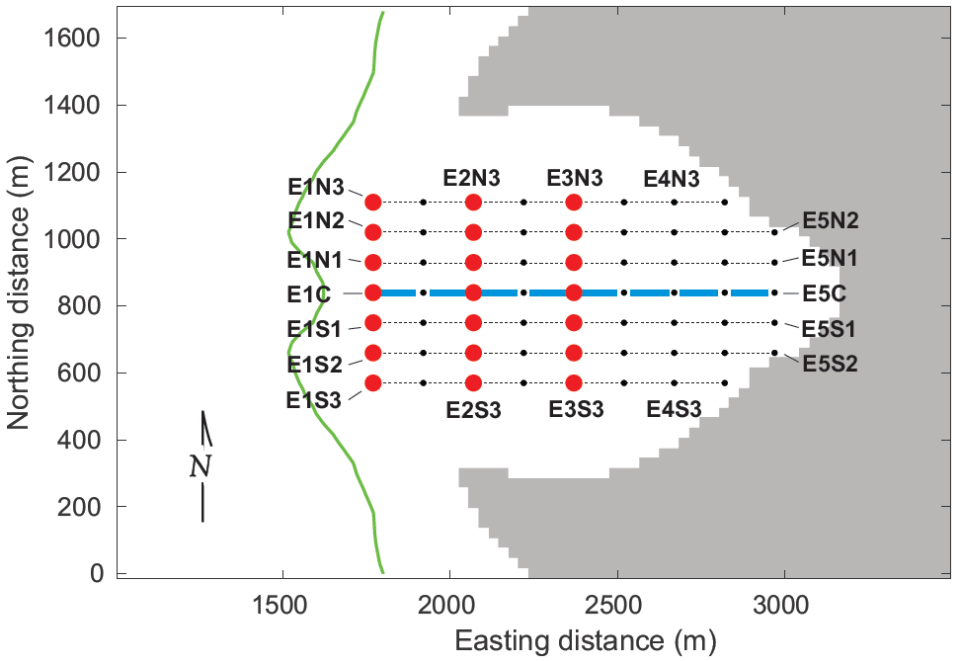

Figure 7. Location of measurement sites for the suite of Traplike simulation models. There are three transverse (north–south) measurement lines: E1, E2, and E3; each transverse line has a centerline site, e.g., E1C and offsets to the north and south, e.g., E1N1, E1N2, and E1N3. Primary sites are indicated by red markers and secondary sites by black dots. The centerline is plotted as a blue line and the ELA as a green curve. The glacier margin is for the Traplike reference model viewed immediately after a surge termination (year 13 of the surge cycle or 1998 in calendar years).

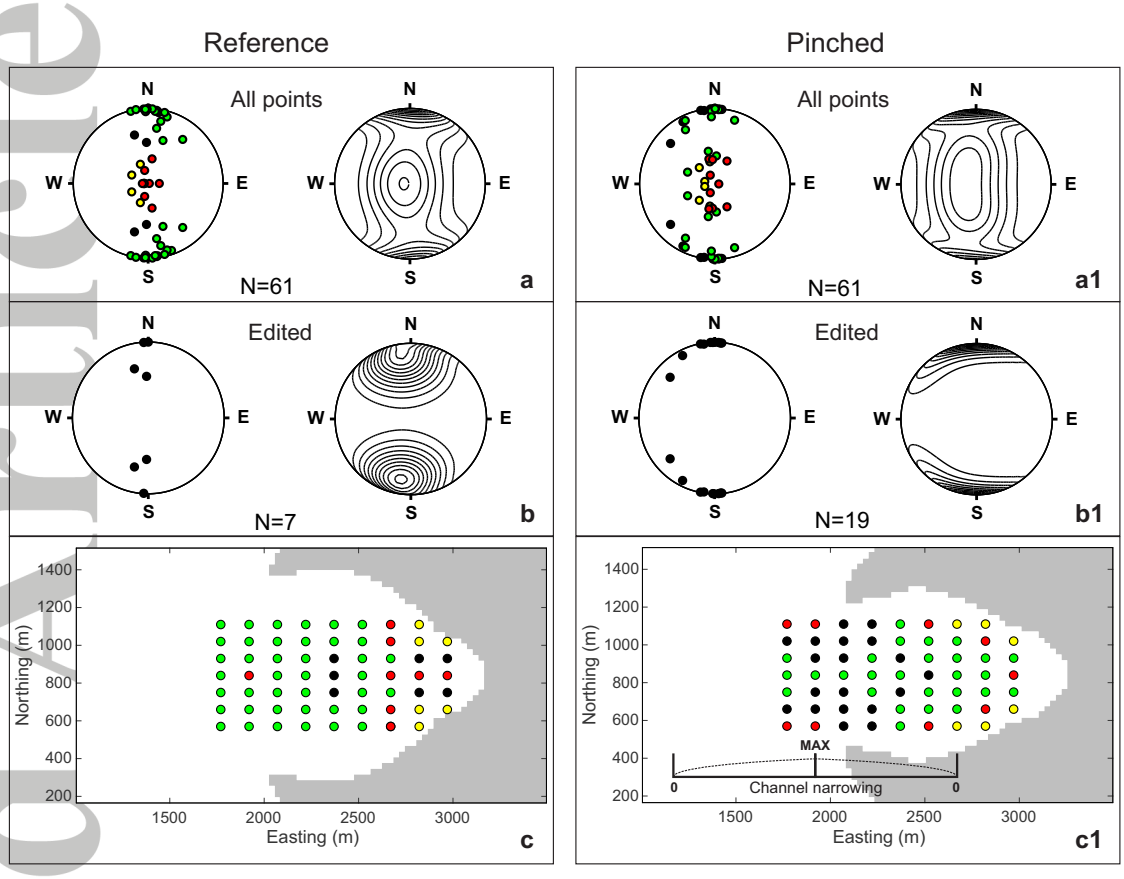

Figure 8. Stereographic projections of the simulated orientation of the S_1 foliation for Traplike Glacier models. The observation year is 2006.6 (year 21.6 of the modeled surge cycle). (a) Reference model (all points). (b) Reference model (edited points). (c) Map of S_1 simulation sites for reference model. (a1) Pinched channel model (all points). (b1) Pinched channel model (edited points). (c1) Map of S_1 simulation sites for pinched channel model. For points, the fill colors indicate whether the point passes all our criteria for S_1 development (black fill) or fails because the dip angle is less than 30° (yellow), or the axis ratio $\kappa_{2:3}$ is less than 5 (green), or both (red).

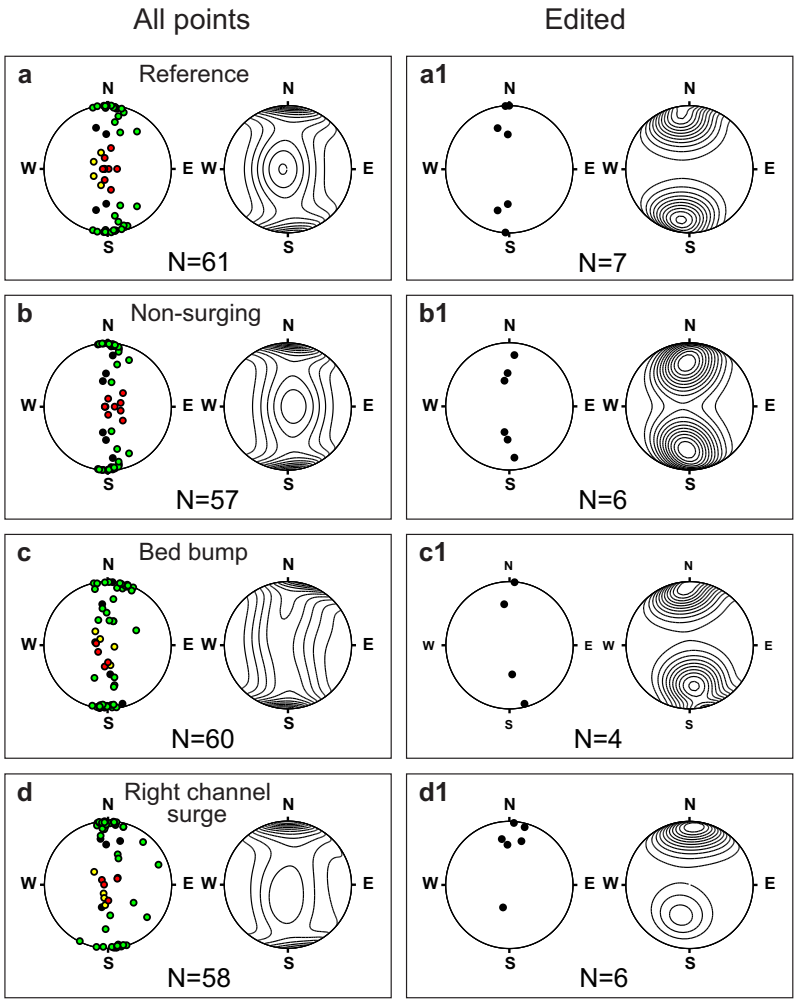

Figure 9. Stereographic projections of simulated orientation of the S_1 foliation for Traplike Glacier models. The observation year is 2006.6 (year 21.6 of the modeled surge cycle). (a) Reference model (all points). (b) Non-surging model (all points). (c) Bed bump model (all points). (d) Right channel surge model (all points). (a1) Reference model (edited). (b1) Non-surging model (edited). (c1) Bed bump model (edited). (d1) Right channel surge model (edited). For points, the fill colors indicate whether the point passes all criteria for S_1 development (black fill) or fails because the dip angle is less than 30° (yellow), or the axis ratio $\kappa_{2:3}$ is less than 5 (green), or both (red).

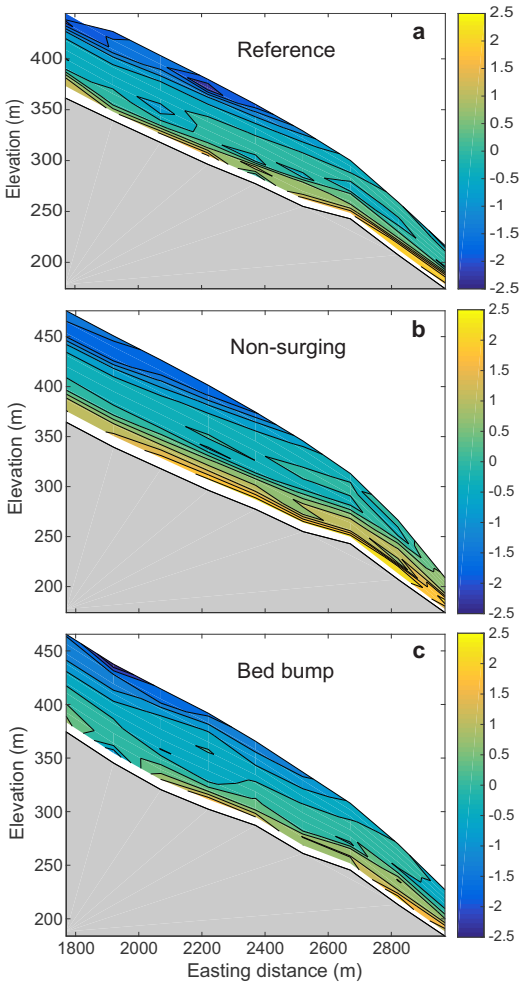

Figure 10. Centerline profiles of $\log_{10} \mathcal{Q}_2$, where $\mathcal{Q}_2$ is a parameter used to characterize the intensity of folding, for Traplike Glacier models and observation year 2006.6 (year 21.6 of the modeled surge cycle). (a) Reference model. (b) Non-surging model. (c) Bed bump model.

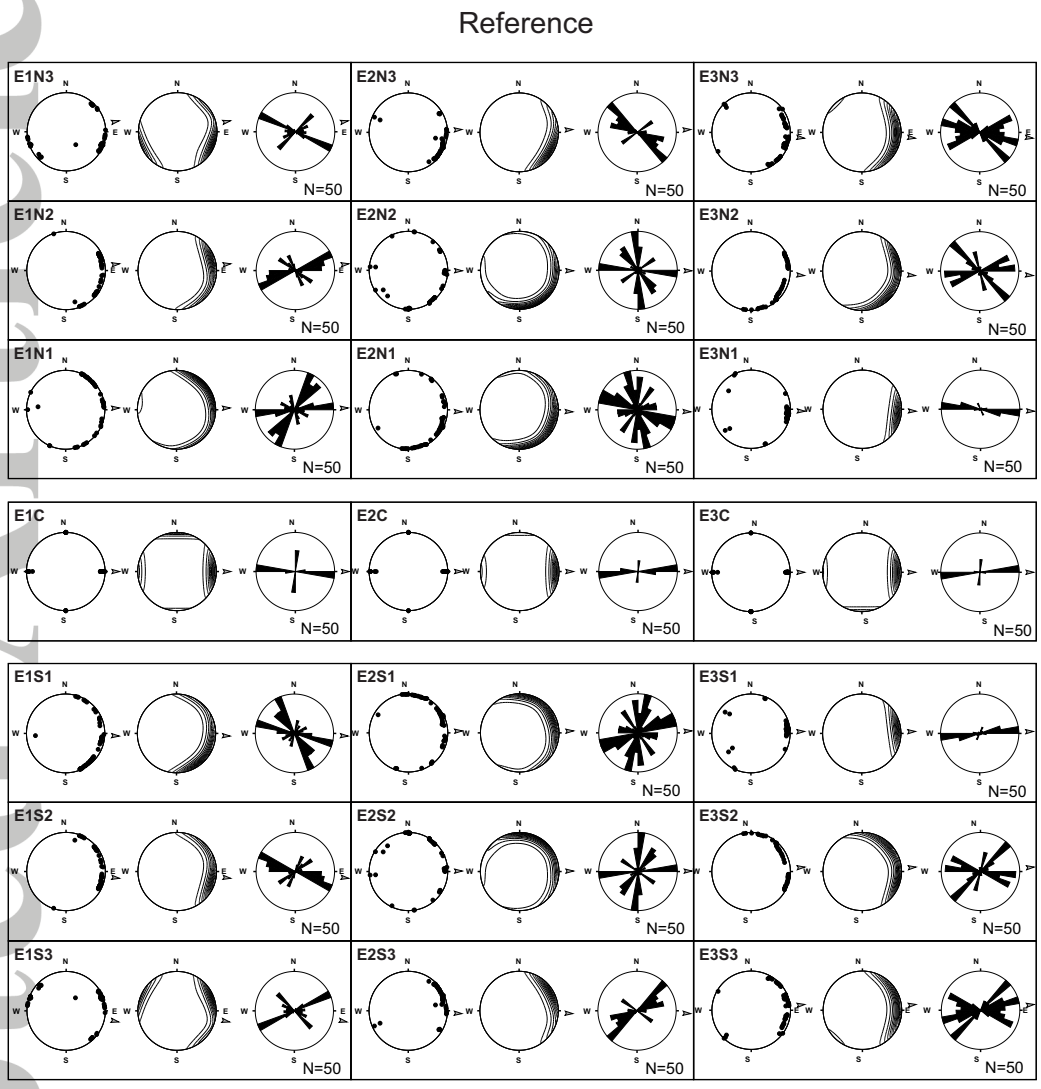

Figure 11. Simulated orientation of surface cracks at 21 sites for Traplike reference model and observation year 2006.6 (year 21.6 of the modeled surge cycle). Each panel shows simulation results in the form of a Schmidt diagram (equal-area, lower hemisphere projections of poles of crevasse traces), a contoured point density plot of the same data, and a rose diagram of the dip directions of the crevasse traces.

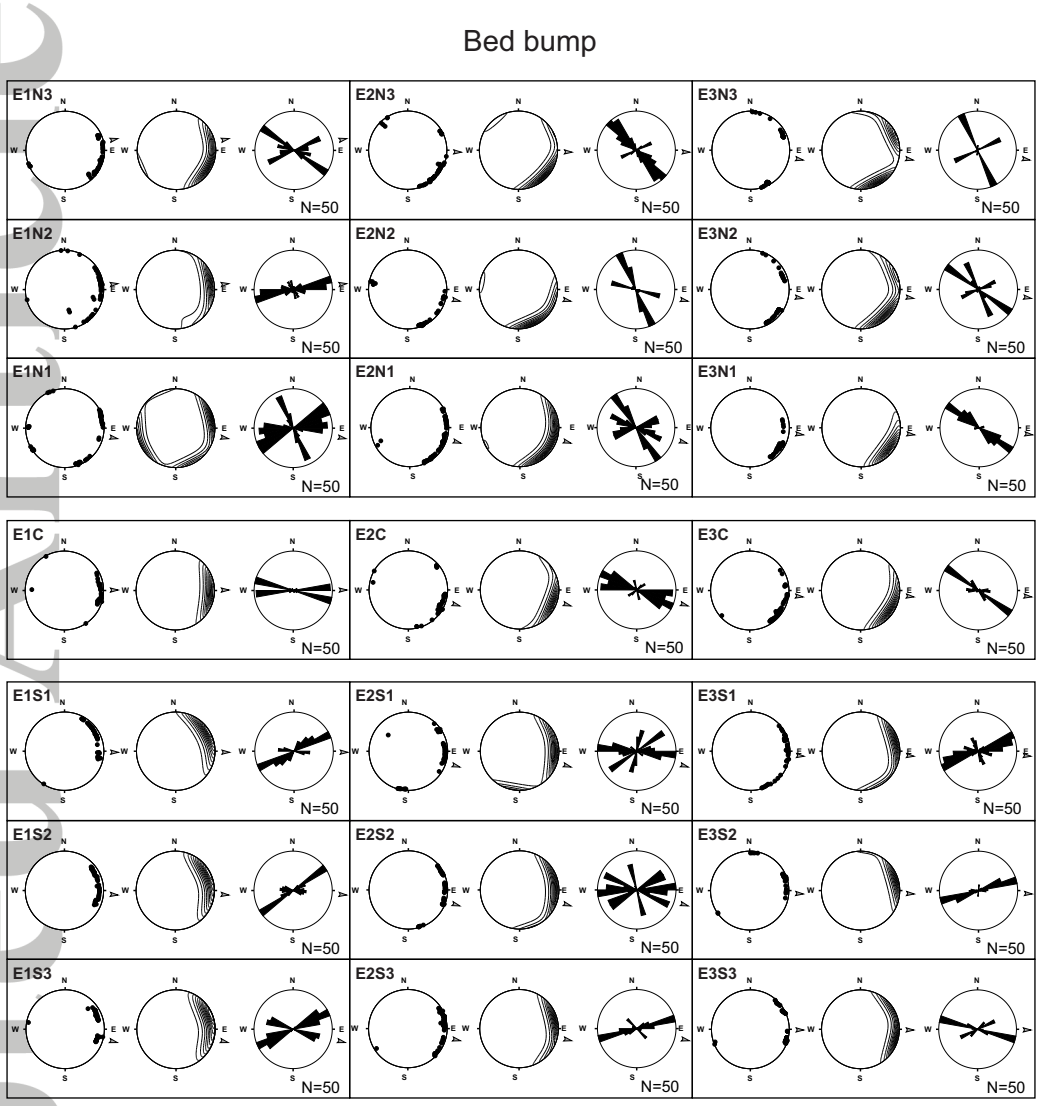

Figure 12. Simulated orientation of surface cracks at 21 sites for Traplike bed bump model and observation year 2006.6 (year 21.6 of the modeled surge cycle). Each panel shows simulation results in the form of a Schmidt diagram (equal-area, lower hemisphere projections of poles of crevasse traces), a contoured point density plot of the same data, and a rose diagram of the dip directions of the crevasse traces.

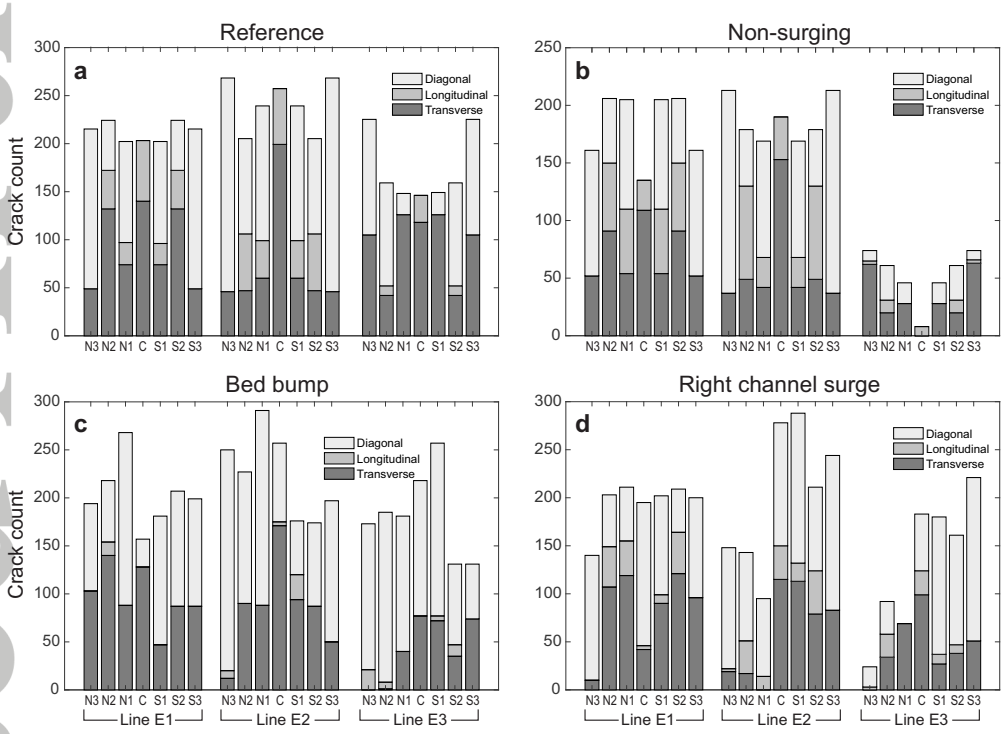

Figure 13. Simulated density and orientation of surface cracks at 21 sites for Traplike Glacier models. The observation year is 2006.6 (year 21.6 of the modeled surge cycle). (a) Reference model. (b) Non-surging model. (c) Bed bump model. (d) Right channel surge model.

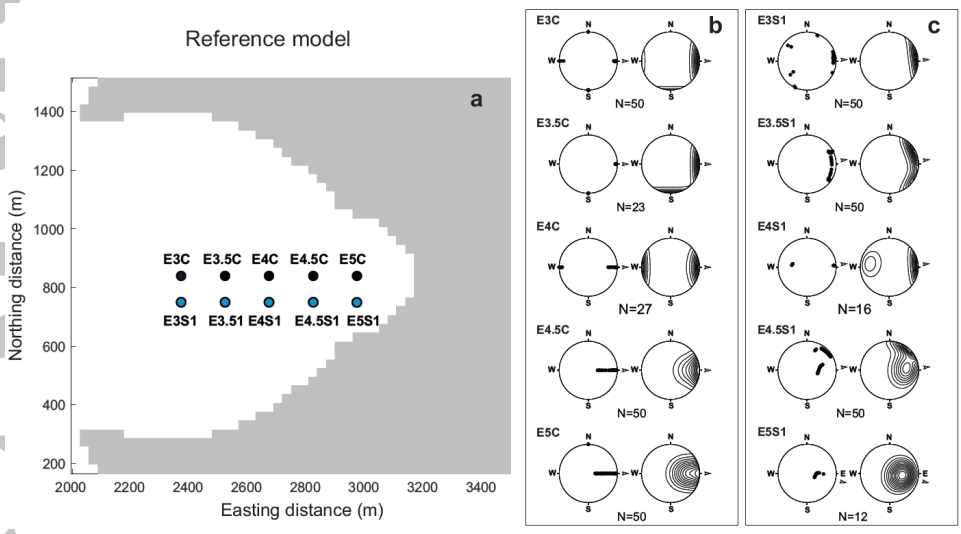

Figure 14. Simulated orientation of surface cracks at centerline (black markers) and southline (blue markers) sites near the glacier terminus for reference model. The observation year is 2006.6 (year 21.6 of the modeled surge cycle). Near the terminus the crack planes are transverse to ice flow and dip up-glacier, as for the transverse S_2 foliation identified in *Hambrey & Clarke* [2019]. (a) Map showing site locations. (b) Schmidt diagrams (equal-area, lower hemisphere projections of poles of crevasse traces) and contoured point density plots for the centerline sites. (c) Schmidt diagrams and contoured density plots for southline sites.